Search for direct production of electroweakinos in final states with one lepton, jets and missing transverse momentum and in pp collisions at $\sqrt{s}$ = 13 TeV with the ATLAS detector

The ATLAS Collaboration

Two searches for electroweak production of chargino-neutralino, $\tilde{\chi}_1^\pm \tilde{\chi}_2^0$, and chargino-chargino, $\tilde{\chi}_1^+ \tilde{\chi}_1^-$, pairs are presented. In both scenarios the chargino decays into a W boson and the lightest neutralino $\tilde{\chi}_1^\pm \to W^\pm \tilde{\chi}_1^0$, and second-to-lightest neutralino decays into a Z boson and the lightest neutralino $\tilde{\chi}_2^0 \to Z \tilde{\chi}_1^0$. The signal signature for both processes is characterized by a single isolated lepton, at least two jet, and missing transverse energy. The searches use 139 fb^{-1} of $\sqrt{s}$ = 13 TeV proton–proton collisions data collected by the ATLAS detector at the Large Hadron Collider between 2015 and 2018. The searches observed no deviation with respect to the Standard Model expectations, and exclusion limits have been set in the $(m(\tilde{\chi}_1^\pm / \tilde{\chi}_2^0), m(\tilde{\chi}_1^0))$ mass plane. For the $\tilde{\chi}_1^+ \tilde{\chi}_1^-$ model, chargino masses ranging from 260 to 520 GeV can be excluded for a massless $\tilde{\chi}_1^0$ at 95% CL, while for the $\tilde{\chi}_1^\pm \tilde{\chi}_2^0$ process, degenerate chargino/neutralino masses ranging from 260 to 420 GeV can be excluded for a massless $\tilde{\chi}_1^0$ at 95% CL.

1 Introduction

The Standard Model (SM) is a strongly predictive theory, yet this theory is not able to completely describe some observed phenomena, such as the abundancy of dark matter, the matter-antimatter asymmetry, and the hierarchy problem. The ATLAS and CMS discovery of the SM Higgs boson [1–4] confirmed the electroweak symmetry breaking mechanism and heightened the attention on the hierarchy problem [5–8]. Supersymmetric (SUSY) [9–14] extensions of the SM can solve the hierarchy problem by introducing a second Higgs boson doublet and a new symmetry which predicts a new boson (fermion) supersymmetric partner for each fermion (boson) of the SM. In an R-parity [15] conserving model, the SUSY particles are produced in pairs and the light SUSY particle (LSP) is a viable dark-matter candidate [16, 17], as it is stable and weakly interacting.

The SUSY partner of the SM Higgs boson (h), and the SM gauge bosons, collectively called electroweakinos, are the higgsinos, winos (partners of the $SU(2)_L$ gauge fields), and bino (partner of the $U(1)$ gauge field). The electroweakino mass eigenstates are linear combinations of higgsino, wino, and bino fields, and are referred to as charginos $\tilde{\chi}_i^\pm$ ($i = 1, 2$) and neutralinos $\tilde{\chi}_j^0$ ($j = 1, 2, 3, 4$) where the states are ordered by increasing value of their mass. Natural SUSY scenarios [18, 19] predict the lightest electroweakino mass to be close to the the electroweak scale. If strongly interacting SUSY particles are heavier than a few TeV, the dominant SUSY production mechanism at the Large Hadron Collider (LHC) may be the direct production of electroweakinos.

In this note we present the results of the searches for two different SUSY processes: $\tilde{\chi}_1^\pm \tilde{\chi}_2^0$ and $\tilde{\chi}_1^+ \tilde{\chi}_1^-$ pair production and their decay into electroweak bosons and the LSP. In both scenarios the lightest chargino ($\tilde{\chi}_1^\pm$) and next-to-lightest neutralino ($\tilde{\chi}_2^0$) are wino-like and nearly mass degenerate, while the LSP ($\tilde{\chi}_1^0$) is a bino-like particle. In these scenarios the lightest chargino and next-to-lightest neutralino can decay via $\tilde{\chi}_1^\pm \to W\tilde{\chi}_1^0$ and $\tilde{\chi}_2^0 \to Z\tilde{\chi}_1^0$ respectively [20–22], and the lepton superpartners are considered to be decoupled. SUSY models with light electroweakinos and light sleptons can also explain the observed discrepancy in the $g - 2$ measurement with respect to the SM predictions [23, 24].The searches for chargino-chargino and chargino-neutralino pair production are performed using proton–proton (pp) collisions produced at the LHC at $\sqrt{s} = 13$ TeV.

The target signature, in both scenarios, is represented by a single isolated light lepton (electron or muon) produced by a W decay, or by taus produced in W decays; two or more jets, which are produced by the hadronic decay of either a W (in the chargino-chargino scenario) or a Z (in the chargino-neutralino scenario), and missing transverse momentum (p_T^{miss}) from LSP and neutrinos. Due to the large momentum carried by the intermediate bosons the jets are expected to behave in semi-boosted, or fully boosted regimes. A set of simplified SUSY models [25, 26] is used to optimise the search and interpret the results. In these models the branching ratios of $\tilde{\chi}_1^\pm \to W\tilde{\chi}_1^0$ and $\tilde{\chi}_2^0 \to Z\tilde{\chi}_1^0$ are assumed to be 100%. The branching ratios of W and Z bosons follow the SM predictions. The diagrams of the processes under consideration are shown in Figure 1.

Previous searches for electroweakino production at the LHC targeting WW and WZ intermediate states, and different lepton multiplicity in the final states, have been reported by the ATLAS [27–31] and CMS [32] collaborations. This analysis is the first ATLAS search targeting final states with exactly one lepton, and profiting from the use of jet-substructure information for W and Z boson identification in large-R jets.
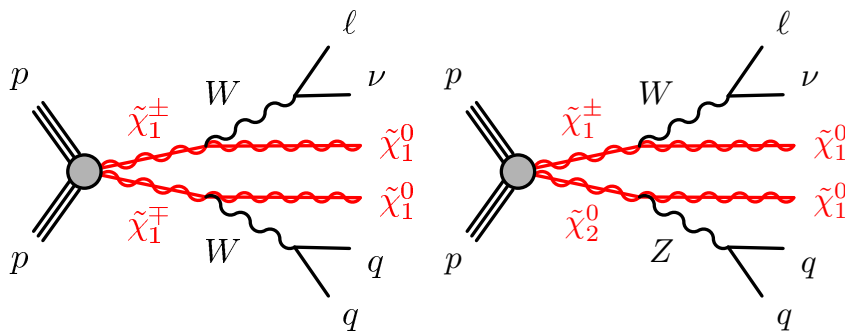
Figure 1: Feynman Diagrams for electroweakino $\tilde{\chi}_1^+ \tilde{\chi}_1^-$ and $\tilde{\chi}_1^\pm \tilde{\chi}_2^0$ pair-production. One $\tilde{\chi}_1^\pm$ decays to a $\tilde{\chi}_1^0$ and a W boson which further decays leptonically. The other $\tilde{\chi}_1^\pm$ or $\tilde{\chi}_2^0$ decays to a $\tilde{\chi}_1^0$ and a W or a Z boson which further decays hadronically.

2 ATLAS detector

The ATLAS detector [33] is a multipurpose particle detector with a nearly 4π coverage in solid angle.[1] It consists of an inner tracking detector surrounded by a thin superconducting solenoid providing a 2 T axial magnetic field, electromagnetic and hadron calorimeters, and a muon spectrometer. The inner tracking detector covers the pseudorapidity range $|\eta| < 2.5$. It consists of silicon pixel, silicon microstrip, and transition radiation tracking detectors. A new inner pixel layer, the insertable B-layer [34, 35], was added at a mean radius of 3.3 cm before the start of 2015 data taking period, improving the identification of b-jets. Lead/liquid-argon (LAr) sampling calorimeters provide electromagnetic (EM) energy measurements with high granularity. A steel/scintillator-tile hadron calorimeter covers the central pseudorapidity range ($|\eta| < 1.7$). The endcap and forward regions are instrumented with LAr calorimeters for EM and hadronic energy measurements up to $|\eta| = 4.9$. The muon spectrometer surrounds the calorimeters and incorporates three large air-core toroidal superconducting magnets with eight coils each. The field integral of the toroids ranges between 2.0 and 6.0 Tm across most of the detector. The muon spectrometer includes a system of precision tracking chambers and fast detectors for triggering. A two-level trigger system [36] is used to select events. The first-level trigger is implemented in hardware and uses a subset of the detector information to keep the accepted rate below 100 kHz. This is followed by a software-based trigger that reduces the accepted event rate to 1 kHz on average depending on the data-taking conditions.

3 Data and simulated events

The searches presented in this paper uses 139 fb^{-1} of pp collision data provided by LHC collected between 2015 and 2018 by the ATLAS detector, at a centre-of-mass energy of 13 TeV and with an interval of 25 ns between consecutive crossings of proton bunches. The average number of interactions per bunch crossing (pile-up) was $\langle\mu\rangle = 20$ in 2015–2016, $\langle\mu\rangle = 38$ in 2017 and $\langle\mu\rangle = 37$ in 2018. The uncertainty in the

---

[1] ATLAS uses a right-handed coordinate system with its origin at the nominal interaction point in the centre of the detector. The positive x-axis is defined by the direction from the interaction point to the centre of the LHC ring, with the positive y-axis pointing upwards, while the beam direction defines the z-axis. Cylindrical coordinates (r, ϕ) are used in the transverse plane, ϕ being the azimuthal angle around the z-axis. The pseudorapidity η is defined in terms of the polar angle θ by $\eta = -\ln\tan(\theta/2)$. Rapidity is defined as $y = 0.5\ln[(E + p_z)/(E - p_z)]$ where E denotes the energy and p_z is the component of the momentum along the beam direction. The angular distance ΔR is defined as $\sqrt{(\Delta\eta)^2 + (\Delta\phi)^2}$.

combined 2015–2018 integrated luminosity is 1.7% [37], obtained using the LUCID-2 detector [38] for the primary luminosity measurements.

Signal selection efficiencies and SM backgrounds were evaluated using Monte Carlo (MC) simulated samples. All simulated samples were produced using the ATLAS simulation infrastructure [39, 40] and GEANT 4 [41], or a faster simulation [42] based on a parameterisation of the calorimeter response and GEANT 4 for the other detector systems. A varying number of inelastic pp interactions was overlaid on the hard-scattering event for all simulated events, in order to model the multiple proton–proton interactions in the same and nearby bunch crossings. The pile-up events are generated with PYTHIA 8.186 [43] using the NNPDF2.3LO set of PDFs [44] and the A3 tune [45]. The simulated events were processed with the same trigger, reconstruction and identification algorithms used for data. Dedicated correction factors are applied to simulation to account for differences between data and MC simulated events.

The simulated backgrounds processes considered in the analyses are: $t\bar{t}$ pair production; single-top production (s-channel, t-channel, and associated Wt production); W/Z+jets production; $t\bar{t}$ production associated with an electroweak boson ($t\bar{t} + V$); Higgs boson production ($t\bar{t} + h$, Vh); diboson (WW, WZ, ZZ) and multiboson (VVV, with $V = W, Z$) production. Diboson and multiboson production involving Higgs bosons are negligible, and they were not simulated. Different MC event generators were used depending on the simulated processes. All simulated background processes were normalised to the best available theoretical calculation of their respective cross-sections. The samples for W and Z boson production associated with jets (W/Z+jets) are generated using SHERPA. The modelling includes up to two partons at NLO, normalized to NNLO for the inclusive cross-section, and five partons at LO using Comix [46] and OpenLoops [47, 48] and merged with the SHERPA parton shower [49] according to the ME+PS@NLO prescription [50–53] using the set of tuned parameters developed by the SHERPA authors. The event generators, the parton shower and hadronisation routines, and the underlying-event parameter tunes and parton distribution function (PDF) sets used in simulating the SM background processes, along with the accuracy of the theoretical cross-sections, are all summarised in Table 1.

For all MC samples showered with PYTHIA, the EvtGen v1.2.0 [54] program was used to simulate the properties of the bottom- and charm-hadron decays. Systematic uncertainties associated with the different background-specific configurations of the MC generators were estimated using MC samples produced without detector simulation. The uncertainties include variations of the renormalisation and factorisation scales, the CKKW-L [55] matching scale, as well as different PDF sets and fragmentation/hadronisation models. A detailed discussion of the uncertainties related to the MC modelling is presented in Section 7.

The SUSY signal samples were generated using MADGRAPH5_aMC@NLO v2.6.2 [56] and PYTHIA 8.230 with the A14 [57] set of tuned parameters for the modelling of the parton showering (PS), hadronisation and underlying event. The matrix element (ME) calculation is performed at tree level and includes the emission of up to two additional partons. The ME–PS matching is done using the CKKW-L prescription, with a matching scale set to one quarter of the chargino and next-to-lightest neutralino mass. The NNPDF2.3LO [44] PDF set was used.

Signal cross-sections are calculated at next-to-leading-order (NLO) accuracy in the strong coupling constant, adding the resummation of soft gluon emission at next-to-leading-logarithm accuracy (NLO+NLL) [58–61]. The nominal cross-section and its uncertainty are taken as the midpoint and half-width of an envelope of cross-section predictions using different PDF sets and factorisation and renormalisation scales, as described in Ref. [62]. The simplified models considered for both scenarios rely on two parameters: for $\tilde{\chi}_1^+ \tilde{\chi}_1^-$ production, they are the masses of the $\tilde{\chi}_1^\pm$ and the $\tilde{\chi}_1^0$; for $\tilde{\chi}_1^\pm \tilde{\chi}_2^0$, they are the masses of $\tilde{\chi}_1^\pm / \tilde{\chi}_2^0$ (considered to be degenerate) and $\tilde{\chi}_1^0$. The production cross-section of both processes decreases as the mass of the $\tilde{\chi}_1^\pm$

Table 1: Simulated background MC samples used in this analysis with the corresponding matrix element and parton shower generators, underlying-event tune, PDF set, and cross-section order in α_s.

Process	Generator	Parton shower and hadronisation	Tune	PDF	Cross-section
$t\bar{t}$	Powheg Box v2 [63–66]	Pythia 8.230 [43]	A14 [57]	NNPDF2.3LO [44]	NNLO+NNLL [67]
Single top	Powheg Box v2 [68–70]	Pythia 8.230	A14	NNPDF2.3LO	NLO+NNLL [71]
W/Z+jets	Sherpa 2.2.11 [72]	Sherpa 2.2.11	Sherpa standard	NNPDF3.0NNLO	NNLO [73]
Diboson	Sherpa 2.2.1 [72] & 2.2.2	Sherpa 2.2.1 & 2.2.2	Sherpa standard	NNPDF3.0NNLO	NLO
Multiboson	Sherpa 2.2.1 & 2.2.2	Sherpa 2.2.1 & 2.2.2	Sherpa standard	NNPDF3.0NNLO	NLO
$t\bar{t} + V$	MadGraph5_aMC@NLO v2.3.3	Pythia 8.210	A14	NNPDF2.3LO	NLO [74]
$t\bar{t} + h$	Powheg Box v2	Pythia 8.230	AZNLO [75]	CTEQ6L1 [76]	NLO [77]
Vh	Powheg Box v2	Pythia 8.212	A14	NNPDF2.3LO	NLO [77]

increases, and for $\tilde{\chi}_1^+ \tilde{\chi}_1^-$ ($\tilde{\chi}_1^\pm \tilde{\chi}_2^0$) ranges from 903 fb (1807 fb) for a 200 GeV $\tilde{\chi}_1^\pm$ mass to 0.62 fb (1.34 fb) for a 1000 GeV $\tilde{\chi}_1^\pm$ mass.

4 Event reconstruction

Events are selected if they have at least one reconstructed pp interaction vertex with two or more associated tracks each with $p_T > 500$ MeV. In case multiple vertices are associated to an event the primary vertex (PV) is defined as the one with the highest scalar sum of the squared transverse momenta of the associated tracks [78]. A set of baseline quality criteria are applied to reject events with non-collision backgrounds or detector noise [79].

Candidate jets and leptons have two levels of classification: 'baseline' and 'signal'. Baseline objects have a lower purity but a higher acceptance and are used for the computation of the missing transverse momentum and solving possible reconstruction ambiguities. Signal objects are a subset of baseline objects and are used in the definition of the regions of interest of the searches.

All electron candidates are reconstructed from energy deposits in the electromagnetic calorimeter that are matched to charged-particle tracks in the inner detector (ID) [80]. Baseline electron candidates are required to have $p_T > 7$ GeV and $|\eta| < 2.47$, and pass the identification requirements of the 'loose' operating point provided by a likelihood-based algorithm, described in Ref. [80]. The longitudinal impact parameter z_0 relative to the PV is required to satisfy $|z_0 \sin\theta| < 0.5$ mm. Discrimination between electrons and converted photons is achieved by observing the number of hits in the innermost pixel layer. Signal electrons are required to satisfy stricter identification criteria: they are required to pass a 'tight' likelihood operating point selection and the significance of the transverse impact parameter d_0 must satisfy $|d_0/\sigma(d_0)| < 5$. Signal electron candidates with $p_T < 75$ GeV are further refined using the *PLVLoose* isolation working point, otherwise they are required to pass the *PLVLTight* isolation working point, as described in Ref. [81].

Muon candidates are reconstructed from matching tracks in the ID and muon spectrometer, refined through a global fit which uses the hits from both subdetectors [82]. Baseline muon candidates are required to have $p_T > 6$ GeV and $|\eta| < 2.7$, the longitudinal impact parameter z_0 relative to the PV is required to satisfy $|z_0 \sin\theta| < 0.5$ mm, and satisfy the 'medium' identification criteria. Signal muon candidates should pass stricter requirements on pseudorapidity and impact parameter, $|\eta| < 2.5$ and $|d_0/\sigma(d_0)| < 3$. Signal muon candidates need to satisfy the *PLVLoose* isolation working point if they have $p_T < 75$ GeV, and the

PflowTightVarRad isolation working point otherwise [81]. Finally a veto is applied on signal muons to reject badly-reconstructed candidates with $\frac{\sigma(q/p)}{(q/p)} > 0.4$.

Jets are reconstructed from three-dimensional topological energy clusters in the calorimeters using the anti-k_t algorithm [83] with a radius parameter $R = 0.4$ [84]. Baseline jet candidates should lie in the $|\eta| < 4.5$ region and have $p_T > 20$ GeV. Signal jets are required to have $|\eta| < 2.8$ and $p_T > 30$ GeV. To suppress jets from pile-up interactions, signal jet candidates with $|\eta| < 2.4$ and $p_T < 60$ GeV have to be matched to the PV through the jet vertex tagger (JVT), a tagging algorithm that identifies jets originating from the PV using track information [85, 86], using the *Tight* working point. Additionally, jets are calibrated following the criteria in Ref. [87], which, among other things, includes corrections to the jet energy and resolution.

In order to exploit the high p_T phase space, large-R jets are used to reconstruct highly boosted bosons by utilising the substructure of collimated objects. Large-R jets are reconstructed with the same algorithm (anti-k_t) as for standard jets, but with a large radius parameter of $R = 1.0$. In order to reduce the pile-up contribution to the large-R a jet trimming algorithm with R_{sub} and f_{cut} parameters set to 0.2 and 0.05 [88], respectively, to identify the parton sub-jets inside the large-R jet. Large-R jets with $p_T > 200$ GeV and $|\eta| > 2.0$ are calibrated using ATLAS prescriptions [89], and are identified as possible W or Z candidates using dedicated taggers designed to identify W and Z bosons at 50% tagging efficiency [90, 91].

Jets originating from the hadronisation of a b quark are identified (b-tagged) via a multivariate algorithm combining information from the impact parameters of displaced tracks as well as topological properties of secondary and tertiary decay vertices reconstructed within the jet. The b-tagging relies on the *DL1r* tagger [92]: the full distribution of the tagger score is used, divided into five bins defined by fixed b-tagging efficiency working points and the distribution edge points (interpreted as the WPs at 100 and 0% efficiency). In the reported searches the *b*-tagged jets are defined using a working point providing a 77% efficiency for *b*-hadron identification in $t\bar{t}$ simulated events. The full score of the *DL1r* tagger is used in a procedure, referred to as pseudo-continuous *b*-tagging, allowing a more fine-grained calibration of the *b*-tagged jets.

To resolve the reconstruction ambiguities between electrons, muons, and jets, an overlap removal procedure is applied to baseline objects. First, any electron sharing the same ID track with a muon is rejected. If it shares the same ID track with another electron, the one with lower p_T is discarded. Next, jets are rejected if they lie within $\Delta R = 0.2$ of a muon or if the muon is matched to the jet through ghost association [93]. Subsequently, electrons within a cone of size $\Delta R = \min(0.4, 0.04 + 10 \text{ GeV}/p_T)$ around a jet are removed. Last, muons within a cone, defined in the same way as for electrons, around any remaining jet are removed.

The missing transverse momentum $\boldsymbol{p}_T^{miss}$, and its magnitude E_T^{miss}, are reconstructed by using the set of reconstructed and fully calibrated baseline objects, i.e. electrons, muons, photons and jets. The baseline electrons, muons and jets are described above. Baseline photons [94] are defined to satify $p_T > 25$ GeV, $|\eta| < 2.37$, and the *tight* identification criteria. The determination of the missing transverse momentum also includes a soft term consisting of tracks that are not associated to any reconstructed object.In the searches described here, the *tight* working point is used for the missing transverse momentum [95, 96].

5 Event selection

Events are recorded with single lepton (electron and muon) triggers [97, 98]. The offline lepton p_T thresholds are set to ensure that the selected events are in the plateau region of the corresponding trigger

efficiency distribution. The trigger p_T threshold values increased over the years due to the increase in luminosity, going from 25 (21) GeV to 27 (27.3) GeV for electron (muon) events.

To target the signal signature, which has one leptonically decaying W boson, one hadronically decaying W or Z boson and large missing energy due to the $\tilde{\chi}_1^0$ and neutrinos escaping detection, events are required to have exactly one signal electron or muon, one to three signal jets and large E_T^{miss}. As one main feature of this analysis is to probe boosted SM boson decays, all events are additionally required to contain at least one large-radius (large-R) jet. Different boson tagging types are employed for different signal scenarios: W-tagging is applied for the chargino-chargino scenario (C1C1-WW), while Z-tagging is applied for the chargino-neutralino scenario (C1N2-WZ).

The signal regions (SR) are then defined using variables which suppress background contributions and increase the sensitivity to the signal. These variables are based on the kinematic properties of the lepton, the jets, and the missing transverse momentum, and are defined as follows:

- The transverse mass, m_T, is defined from the lepton transverse momentum $\boldsymbol{p}_T^\ell$ and the missing transverse momentum $\boldsymbol{p}_T^{miss}$ as

$$m_T = \sqrt{2 p_T^\ell E_T^{miss}(1 - \cos[\Delta\phi(\boldsymbol{p}_T^\ell, \boldsymbol{p}_T^{miss})])}.$$

  where $\Delta\phi(\boldsymbol{p}_T^\ell, \boldsymbol{p}_T^{miss})$ is the azimuthal angle between $\boldsymbol{p}_T^\ell$ and $\boldsymbol{p}_T^{miss}$. For W+jets and semileptonic $t\bar{t}$ events in which one on-shell W boson decays leptonically, this observable has an upper endpoint at the W-boson mass, while for signal events the m_T distribution extends significantly above $m(W)$. A requirement is placed on the upper value of $\Delta\phi(\boldsymbol{p}_T^\ell, \boldsymbol{p}_T^{miss})$ to reject background with a hard lepton and soft jets, where the angle between lepton and $\boldsymbol{p}_T^{miss}$ can be large.

- The effective mass, m_{eff}, is defined as the scalar sum of the lepton transverse momentum, the signal jets transverse momenta, and the missing transverse momentum,

$$m_{eff} = p_T^\ell + \sum_{jets} p_T + E_T^{miss}. \tag{1}$$

  In the design of exclusion SRs, two m_{eff} regions are constructed to target low and high signal mass differences between the $\tilde{\chi}_1^\pm/\tilde{\chi}_2^0$ and the $\tilde{\chi}_1^0$.

- The missing transverse energy significance, $\sigma_{E_T^{miss}}$ [99], is defined as the log-likelihood ratio of measuring the total observed transverse momentum to the likelihood of the null hypothesis,

$$\sigma_{E_T^{miss}} = \sqrt{2\ln\left[\frac{\max_{\boldsymbol{p}_T^{inv}\neq 0}\mathcal{L}\left(E_T^{miss}|\boldsymbol{p}_T^{inv}\right)}{\max_{\boldsymbol{p}_T^{inv}=0}\mathcal{L}\left(E_T^{miss}|\boldsymbol{p}_T^{inv}\right)}\right]}. \tag{2}$$

  A high value indicates that the measured E_T^{miss} value is not compatible with resolution effects only and suggests that the event is more likely to contain objects escaping detection, which happens more in the signal events than the background events.

- The invariant mass of the two leading jets, m_{jj}, is required to be in a range around the W or Z mass for signal events which are expected to emit an on-shell W or Z boson and have a mass peak in the m_{jj} distribution.

An overview of the signal region definitions is provided in Table 2. The main difference between chargino-chargino and chargino-neutralino signal scenarios is the large-R jet boson-tagging type. Three separate classes of signal regions are defined for each scenario, using m_T to target regions sensitive to the increasing mass differences between the $\tilde{\chi}_1^\pm$ (and its mass-degenerate $\tilde{\chi}_2^0$ wino partner) and the $\tilde{\chi}_1^0$. These regions are labelled as **SRLM**, **SRMM** and **SRHM** to indicate low (LM), medium (MM) and high (HM) mass differences, respectively. The requirements on m_T additionally make the three regions mutually exclusive.

The exclusion SRs are designed for setting model-dependent exclusion limits ('excl.'). Each LM, MM and HM SR is further split into two m_{eff} bins, thus providing six bins in total for a simultaneous two-dimensional fit in m_T and m_{eff}. The multi-bin approach enhances the sensitivity to a range of SUSY scenarios with different properties. The missing transverse energy significance is optimized separately for low and high m_{eff} bins. In the low m_{eff} bin, the m_{jj} reconstructed from two resolved jets is required to be within the mass window of the W or Z boson. This is to improve the sensitivity in a semi-boosted regime where the large-R jet would catch most of the boson decay products but oftenly two jets are resolved. The high m_{eff} bin is to target a fully boosted topology thus no additional mass constrain on the resolved jets. For $\tilde{\chi}_1^\pm \tilde{\chi}_2^0$ model, the acceptance times efficiency is 0.37% in SRHM for a 600 GeV $\tilde{\chi}_1^\pm/\tilde{\chi}_2^0$ mass and massless $\tilde{\chi}_1^0$. For $\tilde{\chi}_1^+ \tilde{\chi}_1^-$ model, the acceptance times efficiency is 0.31% in SRMM for a 600 GeV $\tilde{\chi}_1^\pm$ mass and massless $\tilde{\chi}_1^0$.

The discovery SRs are constructed for model-independent limits and null-hypothesis tests ('disc.' for discovery). The various m_{eff} bins are merged for each of the three SRs and selections on m_{jj} and $\sigma_{E_T^{miss}}$ are optimized for the best signal sensitivity on a benchmark point for each m_{eff} bin. The signal and background yield extraction strategy is detailed in Section 6. The systematic uncertainties, fit and results discussed in the following sections are based on the exclusion SRs, while the model-independent results are based on the discovery SRs.

Table 2: Overview of the selection criteria for the exclusion SRs and the discovery SRs. For exclusion SRs, they are further divided into two m_{eff} bins. The selection on m_{jj} and $\sigma_{E_{\text{T}}^{\text{miss}}}$ varies for low and high m_{eff} bins. For discovery SRs, one SR is defined per m_{T} region.

Variable	C1C1-WW model			C1N2-WZ model		
	SRLM	**SRMM**	**SRHM**	**SRLM**	**SRMM**	**SRHM**
N_{lep} ($p_{\text{T}} > 25$ GeV)	1					
N_{jet} ($p_{\text{T}} > 30$ GeV)	$1 - 3$					
$N_{\text{large}-\text{Rjet}}$ ($p_{\text{T}} > 250$ GeV)	≥ 1					
$E_{\text{T}}^{\text{miss}}$ [GeV]	> 200					
$\Delta\phi(\ell, E_{\text{T}}^{\text{miss}})$	< 2.6					
large-R jet type	W-tagged			Z-tagged		
m_{T} [GeV]	120–200	200–300	> 300	120–200	200–300	> 300
	Exclusion SR					
m_{eff} [GeV] (excl.)	[600–850, > 850]			[600–850, > 850]		
m_{jj}[GeV] (excl.)	[70–90, -]			[80–100, -]		
$\sigma_{E_{\text{T}}^{\text{miss}}}$ (excl.)	[> 12, > 15]			[> 12, > 12]		
	Discovery SR					
m_{eff} [GeV] (disc.)	> 600	> 600	> 850	> 600	> 850	> 850
m_{jj}[GeV] (disc.)	-	-	-	80–100	-	-
$\sigma_{E_{\text{T}}^{\text{miss}}}$ (disc.)	> 15	> 15	> 15	> 12	> 12	> 12

6 Background estimation

The dominant SM background sources in the SRs are W+jets (46 - 73%) production, followed by diboson (16 - 39%) and $t\bar{t}$ (2 - 17%) processes. Subdominant SM background contributions originate from Z+jets, single-top, multiboson, $t\bar{t}$ +V, $t\bar{t}$ +h and Vh.

The search uses a partially data-driven technique to estimate the dominant backgrounds. A set of control regions (CR) are designed, where each of the CRs are enriched in one of the dominant background processes. These regions are mutually exclusive and non-overlapping with the SRs. The expected background yield in each SR is determined in a profile likelihood fit, referred to as a 'background-only fit'. With this fit, the normalisation of the major backgrounds is adjusted to match the data in CRs with negligible signal contamination. A probability density function (PDF) is defined for each CR. The inputs are the observed event yield and the predicted background yield from simulation, with Poisson statistical uncertainties as well as with systematic uncertainties (detailed in Section 7) as nuisance parameters. The nuisance parameters are constrained by Gaussian distributions with widths corresponding to the sizes of the uncertainties. Systematic uncertainties account for bin-to-bin correlations, with normalisation and nuisance parameters correlated in all regions. The product of all the PDFs forms the likelihood. The likelihood is maximised by adjusting the normalisation and nuisance parameters. The resulting normalisation factors are then used to correct the expected yields of the corresponding backgrounds in the various SRs. The extrapolation of the adjusted normalisation and nuisance parameters to the SRs is checked in validation regions (VR), which kinematically resemble the SRs but are expected to have low signal contamination, and do not overlap with either CRs or SRs.

For the diboson background, single-lepton processes ($l\nu\nu\nu$) and di-lepton processes ($ll\nu\nu$) contribute evenly to the backgrounds in the signal regions. The $l\nu\nu\nu$ ($ll\nu\nu$) process is marked as diboson1l (diboson2l) in the following yields tables and kinematic figures. The diboson $ll\nu\nu$ entering in the SRs are events with two real leptons present in the decay chain, where one lepton failed the signal lepton requirement, or escaped detection. The $ll\nu\nu$ background is estimated and validated in the two-lepton control and validation regions. The crucial variable to reduce the diboson background contribution is the di-lepton invariant mass, which is required to be in a range around the SM Z boson mass. Furhter selection criteria on E_T^{miss}, $\sigma_{E_T^{miss}}$, and $\Delta\phi(p_T^\ell, p_T^{miss})$ are defined similarly to the SRs, but with less stringent bounds to allow for more statistics. An additional veto on the m_{jj} variable is placed to minimize the potential overlap with a concurrent chargino and neutralino search with two leptons and two jets in the final states done by ATLAS experiment [28], to allow future statistical combinations of different channels targeting the same SUSY production processes. On top of the above selections, the control region **DB2LCR** requires m_T within $50 - 200$ GeV and the validation region **DB2LVR** requires m_T within $200 - 350$ GeV .

The single-lepton diboson process $l\nu\nu\nu$ has one lepton and missing energy in the final state, the kinematic behavior of which is identical to W+jets background. A set of shared control and validation regions, the **WDB1L** regions, are designed for these two processes. The CR is defined with a selection similar to the SRs, but with m_T within $50 - 80$ GeV and with inverted $\sigma_{E_T^{miss}}$ requirements. A b-jet veto is applied to reduce heavy flavor contamination. Two sets of VRs are defined: the **VR1** validates the extrapolation from the CR to the SRs in m_T, and the **VR2** validates the extrapolation from the CR to the SRs in $\sigma_{E_T^{miss}}$ and m_T. The control and validation regions share the same m_{eff} binning as the signal regions. The $t\bar{t}$ control and validation regions, namely **TCR**, **TVR1**, and **TVR2**, have the same selections as the **WDB1L** regions, except for the requirement of at least one b-tagged jet.

A summary of all CR and VR selection criteria is reported in Tables 3 and 4. The W+jets ($l\nu\nu\nu$) purity is 42 - 56% (13 - 21%) in **WDB1LCR**. The $t\bar{t}$ purity is 58 - 77% in **TCR** and $ll\nu\nu$ purity is 58% in **DB2LCR**.

Table 3: Overview of the CR and VR definitions for W+jets, diboson $l\nu\nu\nu$ and $t\bar{t}$ backgrounds. They share the same CR and VR definitions except for number of b-tagged jets requirement. The m_{T} variable provides the orthogonality to the SR.

Variable	**WDB1L** and **T**		
	CR	**VR1**	**VR2**
N_{lep} ($p_{\mathrm{T}} > 25$ GeV)	1		
N_{jet} ($p_{\mathrm{T}} > 30$ GeV)	1 - 3		
$N_{\mathrm{b-jet}}$ ($p_{\mathrm{T}} > 30$ GeV)	0 for WDB1L; > 0 for Top		
$N_{\mathrm{large-Rjet}}$ ($p_{\mathrm{T}} > 250$ GeV)	≥ 1		
$E_{\mathrm{T}}^{\mathrm{miss}}$ [GeV]	> 200		
$\Delta\phi(\ell, E_{\mathrm{T}}^{\mathrm{miss}})$	< 2.9		
large-R jet type	W-tagged		
m_{eff} [GeV]	[600-850,> 850]		
$\sigma_{E_{\mathrm{T}}^{\mathrm{miss}}}$	< 12	< 12	> 12
m_{T} [GeV]	$50 - 80$	> 80	$50 - 120$

Table 4: Overview of the CR and VR definitions for diboson $ll\nu\nu$ backgrounds. The N_{lep} variable provides the orthogonality to the SR.

Variable	**DB2L**	
	CR	**VR**
N_{lep} ($p_{\mathrm{T}} > 25$ GeV)	2	
N_{jet} ($p_{\mathrm{T}} > 30$ GeV)	1 - 3	
$N_{\mathrm{b-jet}}$ ($p_{\mathrm{T}} > 30$ GeV)	0	
$E_{\mathrm{T}}^{\mathrm{miss}}$ [GeV]	> 200	
$\Delta\phi(\ell, E_{\mathrm{T}}^{\mathrm{miss}})$	< 2.9	
$m_{\ell\ell}$ [GeV]	$70 - 100$	
m_{jj}veto [GeV]	$75 - 95$	
$\sigma_{E_{\mathrm{T}}^{\mathrm{miss}}}$	> 12	> 10
m_{T} [GeV]	$50 - 200$	$200 - 350$

Sub-dominant background processes, such as Z+jets, single-top, multiboson, $t\bar{t}$ +V, $t\bar{t}$ +h and Vh, which have no dedicated control regions, are normalised to the cross-sections indicated in Table 1. In the same way as for the dominant backgrounds, their expected yields in the SRs are subject to statistical and systematic uncertainties. Backgrounds with fake leptons such as jets misreconstructed as a lepton, and events with leptons originating from a jet produced by heavy-flavour quarks or from photon conversions, are estimated using a matrix method as described in Ref. [100], and found to be negligible in all regions.

7 Systematic uncertainties

The background yield in the SRs is affected by theoretical and experimental systematic uncertainties. The source of these systematic uncertainties for all simulated signal and background processes are evaluated and presented in this section. The considered theoretical uncertainties are profiled for dominant backgrounds in dedicated control regions, where the systematic uncertainties have just an impact on the the extrapolation factors, while for sub-dominant backgrounds they are entirely estimated from simulation and affect the inclusive cross-section for each process and the acceptance of the analysis selection in all regions.

Theoretical uncertainties for the $t\bar{t}$ and single-top background are further discussed. Single-top and $t\bar{t}$ theoretical uncertainties take into account uncertanties due to the matrix element to parton shower matching, evaluated through a comparison between the nominal Powheg Box +Pythia 8 sample and the alternative aMC@NLO+Pythia 8 sample. Following the same procedure, uncertainties owing to parton shower and hadronisation models derived from comparisons between samples generated with Powheg Box +Pythia 8 and Powheg Box +Herwig 7 [101] are taken into account. The effect of initial- and final- state radiation uncertanties is also evaluated by increasing and decreasing the renormalisation and factorisation scales up and down by a factor of two. The uncertanties assigned to the interference between single-top Wt and $t\bar{t}$ production [102] is obtained by comparing diagram removal (DR) and diagram subtraction (DS) samples, modelled by Powheg Box +Pythia 8.

The diboson modelling uncertainties are studied separately for the single-lepton and the di-lepton processes. They are evaluated by studying the envelope of the seven-point variations of the renormalisation and factorisation scales. Variations of the renormalisation and factorisation scales are also applied to W/Z+jets, multiboson, $t\bar{t}$ +V, $t\bar{t}$ +h, and Vh. The PDF uncertainties are considered following the PDF4LHC15 recommendations [103]. For W/Z+jets, the resummation (QSF) and matching scale (CKKW-L) for the W/Z+jets are estimated by varying the scale parameters up and down for the Sherpa generator. Further, for Sherpa 2.2.11 W/Z+jets samples, the electroweak NLO correction uncertainties are assigned to account for the impact of applying different correction methods. An overall 5% systematic uncertainty in the inclusive cross-section is assigned for the Z+jets samples [104] and similar cross-section uncertainties, 5–10%, are also assigned for other sub-dominant background contributions.

The variations of the parameters corresponding to the factorisation, renormalisation and CKKW-L matching scales in aMC@NLO+Pythia 8 samples provide the uncertainties for the two simplified signal models considered in this analysis.

The experimental uncertainties are related to the jet energy scale (JES), jet energy resolution (JER), E_T^{miss} modeling, lepton reconstruction and identification, pile-up, and JVT. The dominant uncertainties come from JES and JER, which are measured as a function of the p_T and η of the resolved and large-R jet, the pile-up conditions, and the jet flavour composition [105].The uncertainties arising from the large-R jet boson-tagging are grouped into JES and JER systematics uncertainties. The E_T^{miss} modelling systematic errors are estimated by propagating the uncertainties in the energy and momentum scale of each of the objects entering the calculation, and the uncertainties in the soft term's resolution and scale [96]. The evaluation of the lepton reconstruction and identification uncertanties is performed using $Z \rightarrow \ell^+\ell^-$, $J/\psi \rightarrow \ell^+\ell^-$ samples, and $W \rightarrow \ell\nu$ decays [82, 106]. The pile-up uncertainty is computed by performing a 4% up and down variation of the weights associated to $\langle\mu\rangle$.

The dominant systematic uncertainties in the background for the signal regions are presented in Table 5 and 6. The uncertainties in the scale factor fits to the control regions are listed as "Normalisation of dominant backgrounds", contributing around 6 - 7% for each SR. The largest individual experimental uncertainty

Table 5: Breakdown of the dominant systematic uncertainties in background estimates in the various exclusion signal regions for the C1C1-WW model. The individual uncertainties can be correlated, and do not necessarily add up in quadrature to the total background uncertainty. The percentages show the size of the uncertainty relative to the total expected background.

C1C1-WW model	SRLM	SRMM	SRHM
Total background expectation	21.96	9.19	15.65
Total background sytematic	±3.19 [14.54%]	±2.51 [27.29%]	±3.04 [19.40%]
Theoretical systematic uncertainties			
$t\bar{t}$	±1.07 [4.88%]	±0.25 [2.71%]	±0.15 [0.96%]
Single top	±0.31 [1.43%]	±0.08 [0.92%]	±0.35 [2.21%]
W+jets	±0.38 [1.73%]	±0.15 [1.59%]	±0.32 [2.04%]
Diboson	±0.29 [1.34%]	±0.24 [2.66%]	±0.26 [1.63%]
Other backgrounds	±0.10 [0.43%]	±0.07 [0.77%]	±0.08 [0.53%]
MC statistical uncertainties			
MC statistics	±2.09 [9.54%]	±1.61 [17.51%]	±2.07 [13.20%]
Uncertainties in the background normalisation			
Normalisation of dominant backgrounds	±1.48 [6.76%]	±0.62 [6.76%]	±1.12 [7.19%]
Experimental systematic uncertainties			
Jet energy resolution	±1.09 [4.99%]	±1.01 [11.03%]	±1.38 [8.81%]
Jet energy scale	±1.65 [7.51%]	±1.52 [16.54%]	±1.12 [7.19%]
$E_{\mathrm{T}}^{\mathrm{miss}}$	±0.51 [2.34%]	±0.26 [2.80%]	±0.59 [3.76%]
Lepton uncertainties	±0.41 [1.88%]	±0.10 [1.04%]	±0.48 [3.08%]
Pile-up/JVT	±0.10 [0.48%]	±0.21 [2.29%]	±0.23 [1.49%]

amounts to 4-17% depending on the SR. The MC statistical uncertainties contribute $9 - 18\%$ depending on the SR.

Table 6: Breakdown of the dominant systematic uncertainties in background estimates in the various exclusion signal regions for the C1N2-WZ model. The individual uncertainties can be correlated, and do not necessarily add up in quadrature to the total background uncertainty. The percentages show the size of the uncertainty relative to the total expected background.

C1N2-WZ model	SRLM	SRMM	SRHM
Total background expectation	28.53	12.67	17.03
Total background sytematic	±3.68 [12.91%]	±2.54 [20.06%]	±2.85 [16.71%]
Theoretical systematic uncertainties			
$t\bar{t}$	±0.85 [2.97%]	±0.29 [2.33%]	±0.20 [1.18%]
Single top	±1.06 [3.73%]	±0.24 [1.90%]	±0.52 [3.07%]
W+jets	±0.56 [1.97%]	±0.22 [1.76%]	±0.36 [2.10%]
Diboson	±0.48 [1.67%]	±0.24 [1.87%]	±0.58 [3.39%]
Other backgrounds	±0.15 [0.54%]	±0.18 [1.41%]	±0.09 [0.51%]
MC statistical uncertainties			
MC statistics	±2.53 [8.88%]	±1.44 [11.39%]	±2.10 [12.32%]
Uncertainties in the background normalisation			
Normalisation of dominant backgrounds	±1.96 [6.86%]	±0.83 [6.55%]	±1.16 [6.83%]
Experimental systematic uncertainties			
Jet energy resolution	±1.10 [3.85%]	±1.27 [10.03%]	±0.79 [4.63%]
Jet energy scale	±1.28 [4.47%]	±0.99 [7.80%]	±1.25 [7.37%]
$E_\mathrm{T}^\mathrm{miss}$	±0.49 [1.70%]	±0.57 [4.47%]	±0.07 [0.39%]
Lepton uncertainties	±0.34 [1.18%]	±0.23 [1.79%]	±0.20 [1.17%]
Pile-up/JVT	±0.06 [0.20%]	±0.79 [6.24%]	±0.11 [0.63%]

8 Results

The observed event yield in each of the exclusion signal regions is summarised in Table 7 and 8 along with the corresponding SM predictions obtained from the background-only fit. The background normalisation factors are $0.81^{+0.10}_{-0.09}$ for $t\bar{t}$, $1.05^{+0.09}_{-0.09}$ for W+jets and diboson 1L, and $1.22^{+0.18}_{-0.18}$ for diboson 2L.

Figures 2 - 3 present the post-fit m_T, $\sigma_{E_T^{\mathrm{miss}}}$, and m_{eff} distributions compared with the data in the selected control and validation regions. The data and the background expectation in all validation regions agree well within around two standard deviations. Therefore no further systematic uncertainty is applied on the background estimation in the signal regions.

Figure 4 shows the post-fit m_{eff} distributions in SRLM, SRMM, and SRHM for both C1C1-WW and C1N2-WZ models. The uncertainty bands include all statistical and systematic uncertainties. The dashed lines represent the benchmark signal points. The compatibility of the observed and expected event yields in control, validation and exclusion signal regions is illustrated in Figure 5. Mild excesses are seen in some SR targeting the C1N2-WZ model, but no significant excess over the SM prediction is observed in data. Combining the low and high m_{eff} bins of SRMM for C1N2-WZ model leads to a significance of around 2.1σ.

Table 7: Observed event yields and the background expectation obtained by a background fit in the C1C1-WZ model SRs with an integrated luminosity of 139 fb^{-1}. Each column corresponds to a bin in m_{eff}. Uncertainties reported for the fitted background estimates combine statistical (in the simulated event yields) and systematic uncertainties.

C1C1-WW model	SRLM	Bin 0 [600, 850] GeV	Bin 1 > 850 GeV
Observed events	23	16	7
Total SM background events	22.0 ± 3.2	15.8 ± 2.8	6.2 ± 1.0
$t\bar{t}$ events	2.6 ± 1.3	2.2 ± 1.2	0.36 ± 0.21
W+jets events	13.6 ± 2.7	10.1 ± 2.3	3.5 ± 0.8
Z+jets events	$0.10^{+0.16}_{-0.10}$	$0.04^{+0.13}_{-0.04}$	0.054 ± 0.034
Single-top events	0.5 ± 0.4	$0.19^{+0.25}_{-0.19}$	0.26 ± 0.18
Diboson2l events	1.7 ± 0.5	1.3 ± 0.4	0.43 ± 0.12
Diboson1l events	3.0 ± 0.7	1.5 ± 0.5	1.41 ± 0.30
$t\bar{t}$ +V events	0.50 ± 0.14	0.30 ± 0.10	0.20 ± 0.06
$t\bar{t}$ +h events	0.008 ± 0.005	0.005 ± 0.005	0.003 ± 0.001
multiboson events	0.005 ± 0.002	0.0 ± 0.0	0.005 ± 0.002

C1C1-WW model	SRMM	Bin 0 [600, 850] GeV	Bin 1 > 850 GeV
Observed events	11	7	4
Total SM background events	9.2 ± 2.5	6.4 ± 2.2	2.7 ± 0.9
$t\bar{t}$ events	0.60 ± 0.32	0.44 ± 0.25	0.16 ± 0.10
W+jets events	5.3 ± 2.1	4.0 ± 1.9	1.3 ± 0.5
Z+jets events	0.11 ± 0.04	0.09 ± 0.04	0.020 ± 0.010
Single-top events	0.12 ± 0.09	0.09 ± 0.07	$0.03^{+0.03}_{-0.07}$
Diboson2l events	1.4 ± 0.4	0.89 ± 0.32	0.49 ± 0.21
Diboson1l events	1.4 ± 0.4	0.80 ± 0.28	0.64 ± 0.25
$t\bar{t}$ +V events	0.29 ± 0.12	0.16 ± 0.09	0.13 ± 0.07
$t\bar{t}$ +h events	0.004 ± 0.002	0.004 ± 0.002	0.0 ± 0.0
multiboson events	0.0 ± 0.0	0.0 ± 0.0	0.0 ± 0.0

C1C1-WW model	SRHM	Bin 0 [600, 850] GeV	Bin 1 > 850 GeV
Observed events	16	4	12
Total SM background events	15.7 ± 3.0	4.8 ± 1.3	10.8 ± 2.5
$t\bar{t}$ events	0.36 ± 0.18	0.19 ± 0.11	0.17 ± 0.09
W+jets events	11.3 ± 2.5	3.3 ± 1.1	8.0 ± 2.2
Z+jets events	0.17 ± 0.07	0.14 ± 0.06	0.029 ± 0.018
Single-top events	0.49 ± 0.34	0.23 ± 0.17	0.26 ± 0.20
Diboson2l events	1.5 ± 0.4	0.54 ± 0.17	0.99 ± 0.28
Diboson1l events	1.5 ± 0.4	0.39 ± 0.14	1.09 ± 0.31
$t\bar{t}$ +V events	0.33 ± 0.12	0.037 ± 0.035	0.29 ± 0.11
$t\bar{t}$ +h events	0.003 ± 0.003	0.0 ± 0.0	0.003 ± 0.003
multiboson events	0.004 ± 0.001	0.0 ± 0.0	0.004 ± 0.001

Table 8: Observed event yields and the background expectation obtained by a background fit in the C1C1-WW model SRs with an integrated luminosity of 139 fb^{-1}. Each column corresponds to a bin in m_{eff}. Uncertainties reported for the fitted background estimates combine statistical (in the simulated event yields) and systematic uncertainties.

C1N2-WZ model	SRLM	Bin 0 [600, 850] GeV	Bin 1 > 850 GeV
Observed events	26	16	10
Total SM background events	29 ± 4	15.6 ± 2.8	13.0 ± 1.8
$t\bar{t}$ events	2.7 ± 1.0	1.6 ± 0.7	1.1 ± 0.4
W+jets events	18.1 ± 2.8	10.6 ± 2.1	7.5 ± 1.2
Z+jets events	$0.06^{+0.60}_{-0.06}$	$0.03^{+0.66}_{-0.03}$	$0.03^{+0.06}_{-0.03}$
Single-top events	$0.6^{+1.0}_{-0.6}$	$0.16^{+0.34}_{-0.16}$	$0.5^{+0.8}_{-0.5}$
Diboson2l events	2.4 ± 0.6	1.4 ± 0.4	0.96 ± 0.28
Diboson1l events	3.9 ± 0.9	1.3 ± 0.4	2.5 ± 0.6
$t\bar{t}$ +V events	0.74 ± 0.22	0.37 ± 0.13	0.37 ± 0.11
$t\bar{t}$ +h events	0.021 ± 0.006	0.011 ± 0.004	0.010 ± 0.004
multiboson events	0.020 ± 0.005	0.0 ± 0.0	0.020 ± 0.005

C1N2-WZ model	SRMM	Bin 0 [600, 850] GeV	Bin 1 > 850 GeV
Observed events	22	13	9
Total SM background events	12.7 ± 2.5	7.0 ± 2.2	5.7 ± 1.3
$t\bar{t}$ events	0.9 ± 0.4	0.52 ± 0.23	0.41 ± 0.20
W+jets events	7.3 ± 2.0	4.4 ± 1.9	2.9 ± 0.8
Z+jets events	0.30 ± 0.23	0.12 ± 0.12	0.18 ± 0.15
Single-top events	$0.14^{+0.24}_{-0.14}$	$0.09^{+0.16}_{-0.09}$	$0.05^{+0.11}_{-0.05}$
Diboson2l events	1.5 ± 0.4	0.66 ± 0.28	0.85 ± 0.25
Diboson1l events	1.9 ± 0.5	0.94 ± 0.27	0.95 ± 0.30
$t\bar{t}$ +V events	0.54 ± 0.17	0.25 ± 0.10	0.28 ± 0.10
$t\bar{t}$ +h events	$0.026^{+0.029}_{-0.026}$	0.005 ± 0.004	$0.022^{+0.025}_{-0.022}$
multiboson events	0.008 ± 0.002	0.004 ± 0.001	0.004 ± 0.001

| C1N2-WZ model	SRHM	Bin 0 [600, 850] GeV	Bin 1 > 850 GeV
Observed events	26	5	21
Total SM background events	17.0 ± 2.8	3.3 ± 1.4	13.7 ± 2.3
$t\bar{t}$ events	0.63 ± 0.28	0.23 ± 0.15	0.40 ± 0.19
W+jets events	11.6 ± 2.1	2.3 ± 1.1	9.3 ± 1.6
Z+jets events	0.045 ± 0.022	0.076 ± 0.021	0.0 ± 0.0
Single-top events	1.3 ± 0.7	$0.014^{+0.066}_{-0.014}$	1.2 ± 0.7
Diboson2l events	1.5 ± 0.7	0.30 ± 0.18	1.2 ± 0.5
Diboson1l events	1.6 ± 0.4	0.35 ± 0.15	1.22 ± 0.30
$t\bar{t}$ +V events	0.42 ± 0.14	$0.019^{+0.023}_{-0.019}$	0.40 ± 0.14
$t\bar{t}$ +h events	0.003 ± 0.003	0.0 ± 0.0	0.003 ± 0.003
multiboson events	$0.006^{+0.011}_{-0.006}$	0.0 ± 0.0	$0.006^{+0.011}_{-0.006}$

17
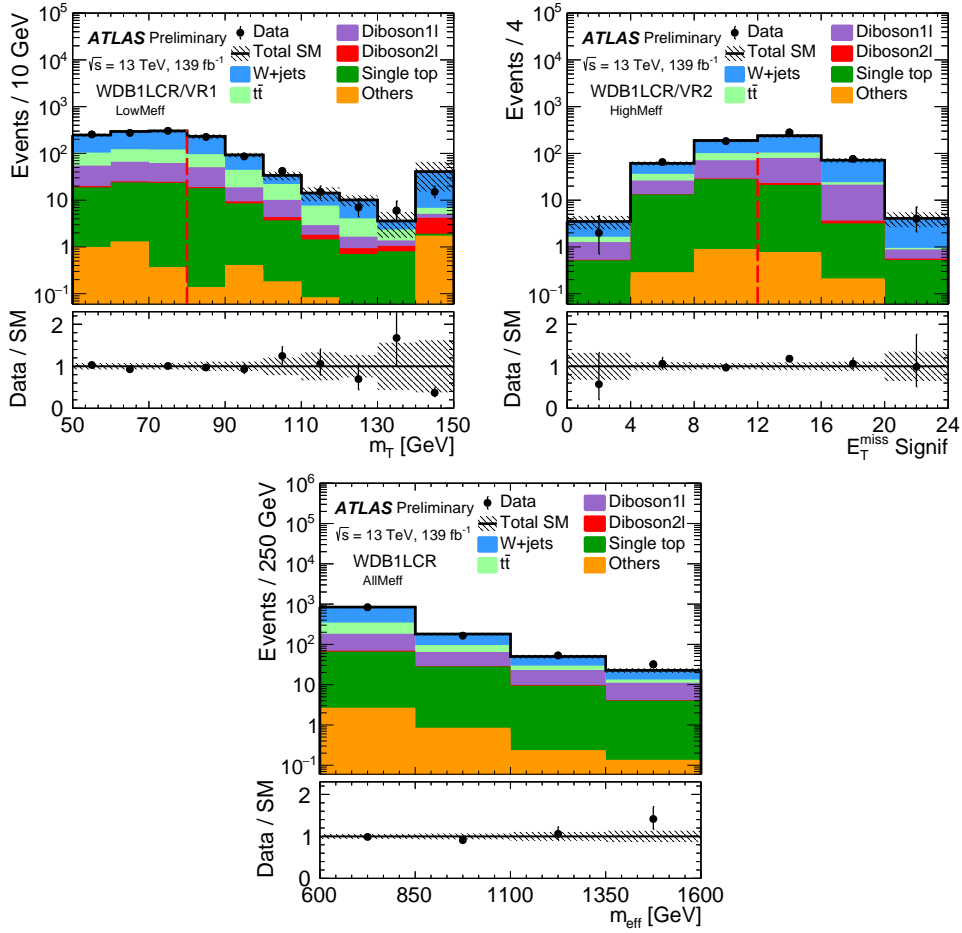
Figure 2: The post-fit (top left) m_T distribution in WDB1L CR and VR1 for low m_{eff} bin, (top right) $\sigma_{E_T^{miss}}$ distribution in WDB1L CR and VR2 for high m_{eff} bin and (bottom) m_{eff} distribution in WDB1L CR are shown. The red dash line separates the control and validation regions. The uncertainty bands plotted include all statistical and systematic uncertainties. The overflow events, where present, are included in the last bin.

Table 9 summarises the observed (S_{obs}^{95}) and expected (S_{exp}^{95}) 95% CL upper limits on the number of signal events and on the observed visible cross-section, $\langle\epsilon\sigma\rangle_{obs}^{95}$, for each SR(disc.). The discovery SRs are used to test for the presence of any beyond-the-Standard-Model (BSM) physics processes. Upper limits on contributions from new physics processes are estimated using the so-called 'model-independent fit', where a generic BSM process is assumed to contribute only to the SR and not to the CRs, thus giving a conservative background estimate in the SR. When normalised to the integrated luminosity of the data sample, the results can be interpreted as corresponding to observed upper limits $\langle\epsilon\sigma\rangle_{obs}^{95}$, defined as the product of the production cross-section, the acceptance, and the selection efficiency of a BSM signal. The p_0 value and the CL_B value are also provided. The former represents the probability of the SM background alone to fluctuate to the observed number of events or higher, and latter provides the confidence level observed for the background-only hypothesis.

Model-dependent exclusion limits at 95% confidence level (CL) are placed on the signal model. These limits are shown as a function of the masses of the supersymmetric particles in Figure 6. A likelihood
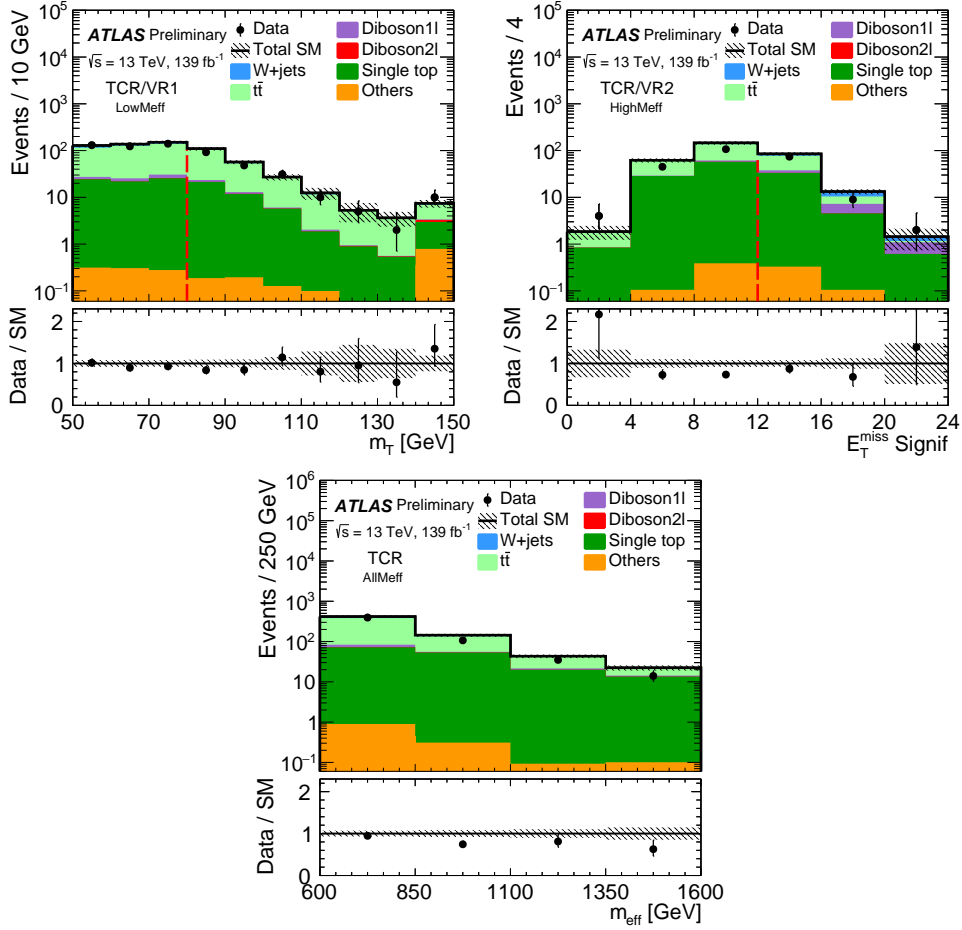
Figure 3: The post-fit (top left) m_T distribution in $t\bar{t}$ CR and VR1 for low m_{eff} bin, (top right) $\sigma_{E_T^{\text{miss}}}$ distribution in $t\bar{t}$ CR and VR2 for high m_{eff} bin and (bottom) m_{eff} distribution in $t\bar{t}$ CR are shown. The red dash line separates the control and validation regions. The uncertainty bands plotted include all statistical and systematic uncertainties. The overflow events, where present, are included in the last bin.
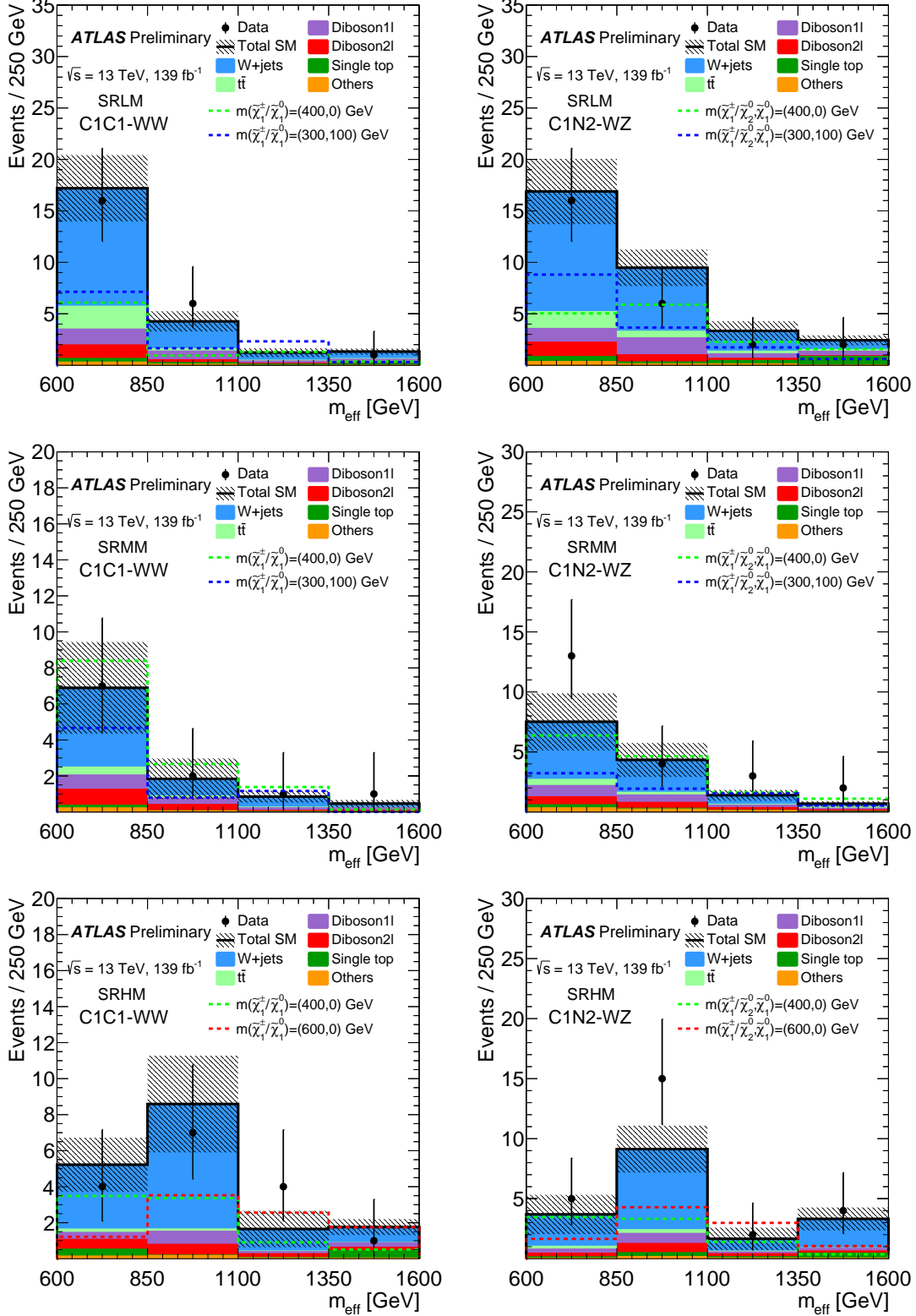
Figure 4: The post-fit m_{eff} distributions in the exclusion signal regions (SRLM, SRMM, and SRHM) for C1C1-WW and C1N2-WZ models. The uncertainty bands plotted include all statistical and systematic uncertainties. The dashed lines represent the benchmark signal samples. The overflow events, where present, are included in the last bin.
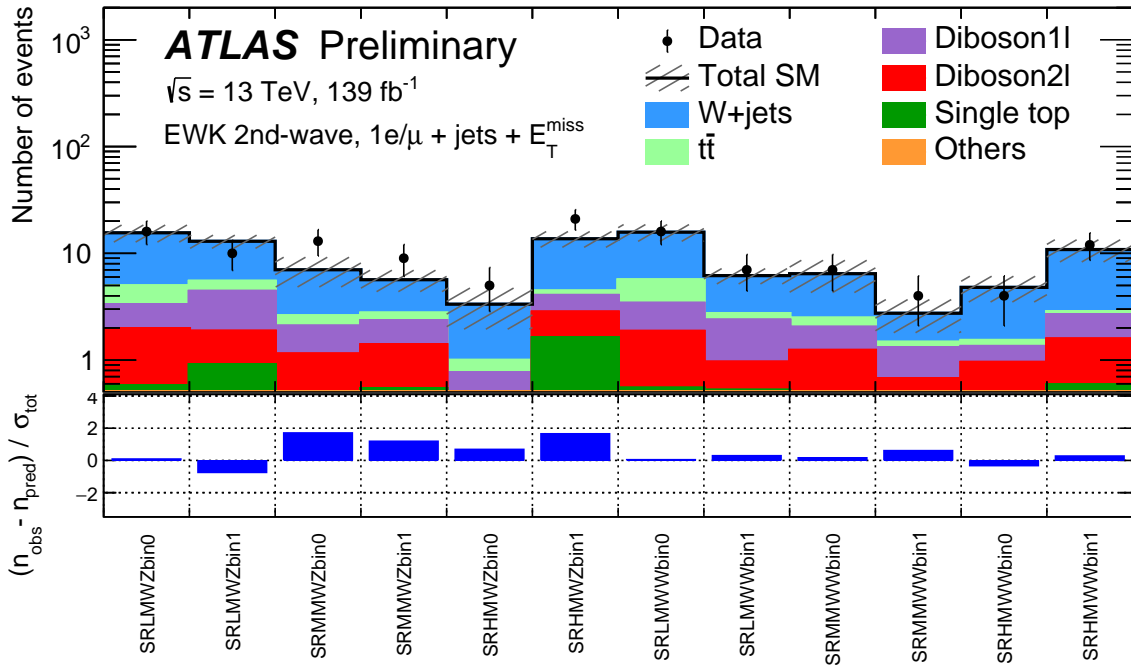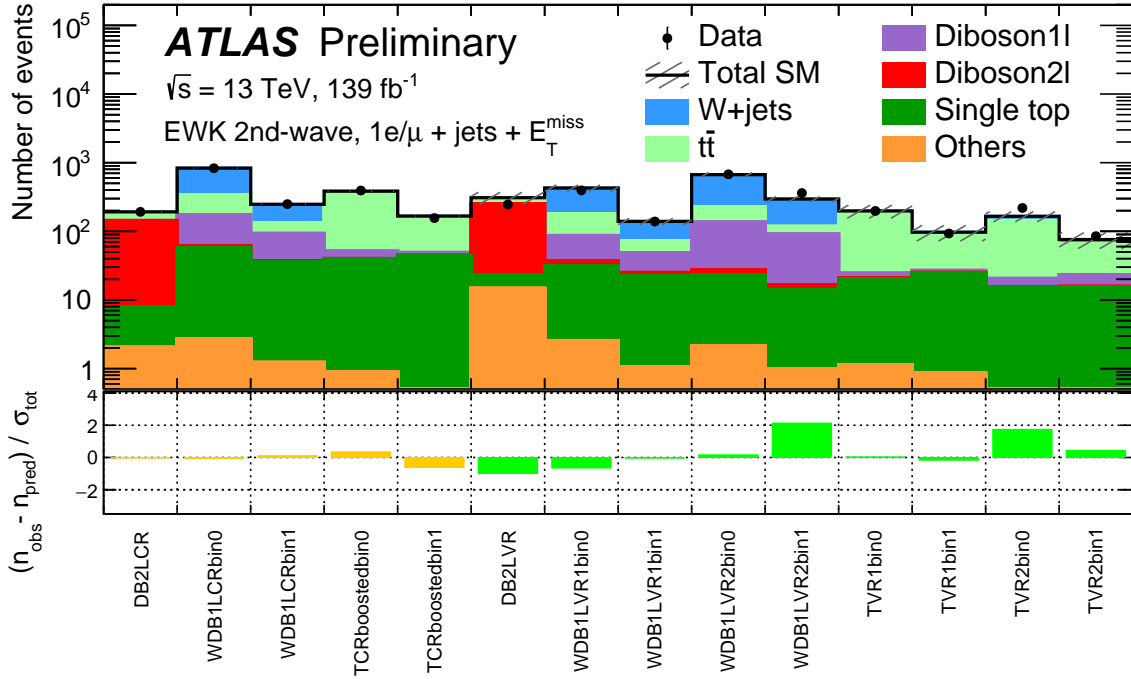
Figure 5: Comparison of the observed and expected event yields in (top) the control and validation regions, and (bottom) the exclusion signal regions. Uncertainties in the background estimates include both the statistical (in the simulated event yields) and systematic uncertainties. The bottom panel shows the significance [107] of the differences between the observed and expected yields and it is depicted in yellow, green and blue colors for control regions, validation regions and signal regions, respectively.

Table 9: Left to right: Observed events, total SM background, 95% CL upper limits on the visible cross section ($\langle\epsilon\sigma\rangle^{95}_{obs}$) and on the number of signal events (S^{95}_{obs}). The fifth column (S^{95}_{exp}) shows the 95% CL upper limit on the number of signal events, given the expected number (and $\pm1\sigma$ excursions on the expectation) of background events. The last three columns indicate the CL_B value and the discovery p-value ($p(s=0)$) with the corresponding gaussian significance (Z). CL_B provides a measure of compatibility of the observed data with the 95% CL signal strength hypothesis relative to fluctuations of the background, and $p(s=0)$ measures compatibility of the observed data with the background-only (zero signal strength) hypothesis relative to fluctuations of the background. Larger values indicate greater relative compatibility. $p(s=0)$ is not calculated in signal regions with a deficit with respect to the nominal background prediction.

Signal channel	Observed events	Total SM background	$\langle\epsilon\sigma\rangle^{95}_{obs}$[fb]	S^{95}_{obs}	S^{95}_{exp}	CL_B	p_0	Z
C1C1-WW model								
SRLM (disc.)	16	11.6 ± 1.6	0.09	13.0	$8.8^{+4.3}_{-1.5}$	0.84	0.14	1.09
SRMM (disc.)	9	9.8 ± 2.0	0.06	7.9	$9.0^{+5.4}_{-1.4}$	0.42	0.50	0.00
SRHM (disc.)	12	10.8 ± 2.5	0.07	10.4	$9.4^{+4.1}_{-3.0}$	0.60	0.39	0.29
C1N2-WZ model								
SRLM (disc.)	17	18.4 ± 2.9	0.08	11.5	$13.7^{+4.0}_{-4.5}$	0.40	0.50	0.00
SRMM (disc.)	9	5.7 ± 1.3	0.07	10.2	$6.8^{+3.1}_{-0.9}$	0.87	0.13	1.11
SRHM (disc.)	21	13.7 ± 2.3	0.13	17.5	$10.5^{+4.4}_{-2.4}$	0.92	0.06	1.54

similar to the one used in the background-only fit, but with additional terms for the SRs, is used for the calculation. The exclusion SRs thus participate in the fit and are used to constrain normalisation and nuisance parameters. A signal is allowed in this likelihood in both the CRs and SRs. The VRs are not used in the fit. The CL_s method [108] is used to derive the confidence level of the exclusion for a particular signal model; signal models with a CL_s value below 0.05 are excluded at 95% CL. The uncertainties in the observed limit are calculated by varying the cross-section for the signal up and down by its uncertainty. For the C1N2-WZ model, due to a mild excess observed in several bins of the exclusion signal regions, the observed limit is weaker than the expected limit and excludes the range of $260-420$ GeV in $\tilde{\chi}^\pm_1/\tilde{\chi}^0_2$ mass for massless $\tilde{\chi}^0_1$. The limit in the high $\tilde{\chi}^\pm_1/\tilde{\chi}^0_2$ mass region is dominated by the high m_{eff} bin of SR-HM. For the C1C1-WW model, the $\tilde{\chi}^\pm_1$ mass of about $260-520$ GeV is excluded for massless $\tilde{\chi}^0_1$, which complements an uncovered phase space of around 100 GeV in $m(\tilde{\chi}^\pm_1)$ from the previous ATLAS limits. The previous ATLAS limits covered a lower mass area probed by a 0-lepton analysis [30] and a higher mass area probed by a 2-lepton analysis [29]. The 1-lepton result well cover the intermediate region.
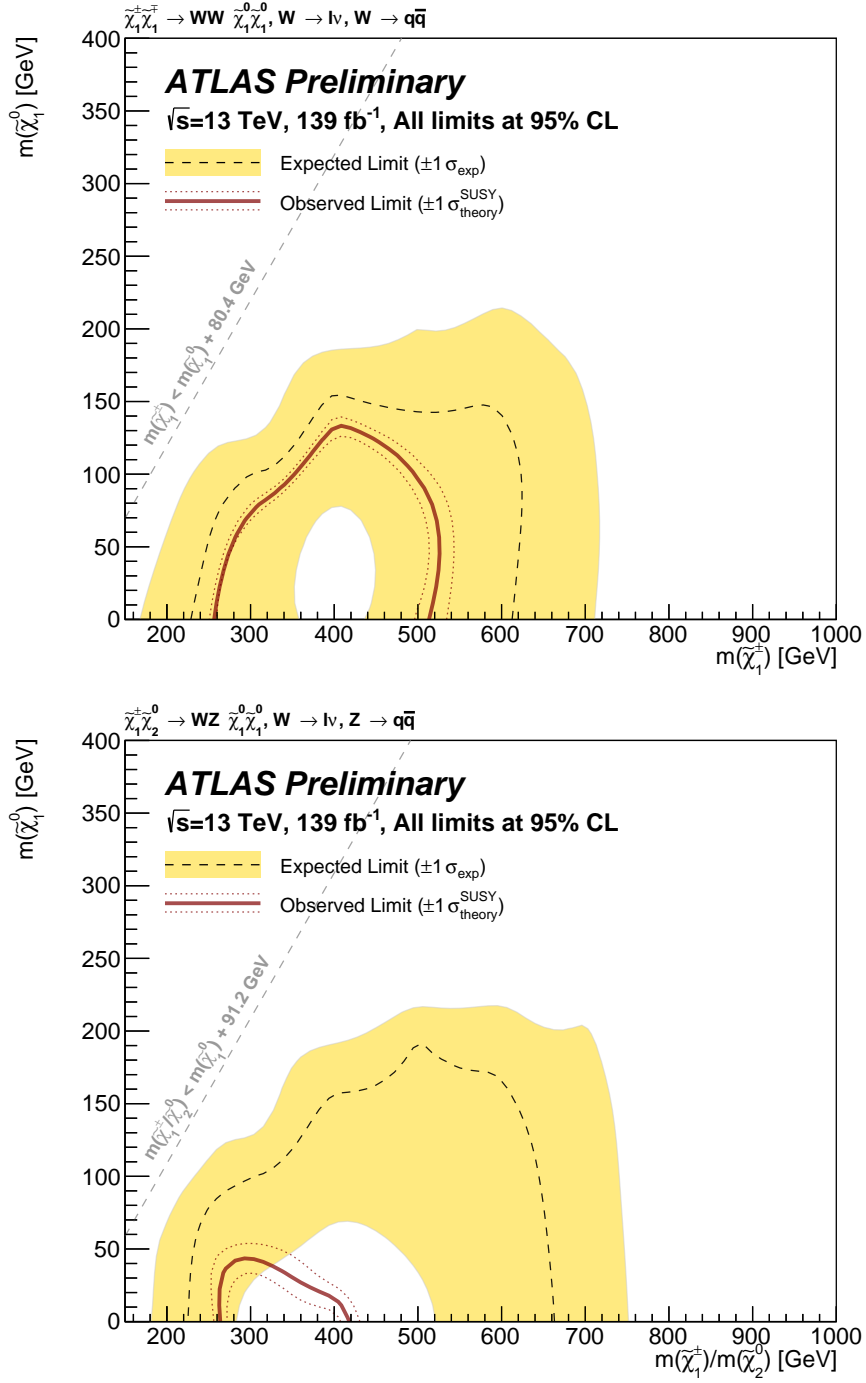
Figure 6: Model-dependent exclusion contour at 95% CL on (top) the chargino pair production and (bottom) the production of a chargino and a next-to-lightest neutralino. The observed limit is given by the solid line with the signal cross-section uncertainties shown by the dotted lines as indicated in the text. Expected limits are given by the dashed line with uncertainties shown by the shaded band.

9 Conclusion

The results of two searches for electroweakino pair production $pp \to \tilde{\chi}_1^\pm \tilde{\chi}_2^0 / \tilde{\chi}_1^+ \tilde{\chi}_1^-$ in which the chargino ($\tilde{\chi}_1^\pm$) decays into a W boson and the lightest neutralino ($\tilde{\chi}_1^0$), while the heavier neutralino ($\tilde{\chi}_2^0$) decays into a Z boson and a second $\tilde{\chi}_1^0$ are presented. The search is performed in events with one isolated lepton, jets and missing transverse momentum, using pp collisions provided by the LHC at a centre-of-mass energy of 13 TeV. Data collected with the ATLAS detector between 2015 and 2018 are used, corresponding to an integrated luminosity of 139 fb^{-1}. No significant deviation from the expected Standard Model background is observed. Limits are set on the direct production of the electroweakinos in simplified models. In the $\tilde{\chi}_1^\pm \tilde{\chi}_2^0$ model, masses of $\tilde{\chi}_1^\pm / \tilde{\chi}_2^0$ ranging from 260 to 420 GeV are excluded at 95% confidence level for a massless $\tilde{\chi}_1^0$. In the $\tilde{\chi}_1^+ \tilde{\chi}_1^-$ model, masses of $\tilde{\chi}_1^\pm$ ranging from 260 to 520 GeV are excluded at 95% confidence level for a massless $\tilde{\chi}_1^0$. The current search improves on the previous ATLAS limit by around 100 GeV in $m(\tilde{\chi}_1^\pm)$ for a massless $\tilde{\chi}_1^0$.

Appendix

More kinematics in control and validation regions are shown in this section. In Figures 7 - 9 the post-fit m_T and $\sigma_{E_\mathrm{T}^\mathrm{miss}}$ distributions in all control regions are compared with the data. Figures 10 - 14 shows the post-fit m_T and $\sigma_{E_\mathrm{T}^\mathrm{miss}}$ distributions after all of the validation region selection requirements. Figure 15 shows the model-dependent exclusion contour at 95% CL on the chargino pair production with a grey shaded areas representing the excluded mass hypotheses from other ATLAS searches.
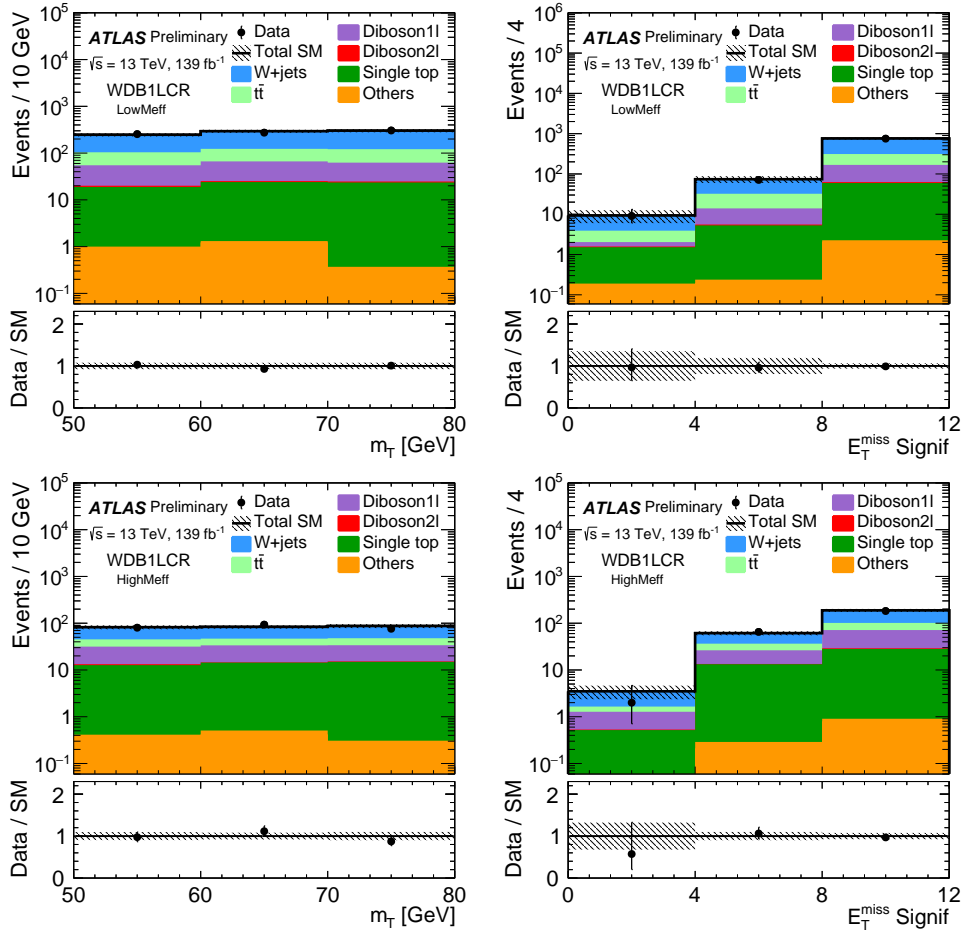
Figure 7: The post-fit m_T and $\sigma_{E_T^{miss}}$ distributions in WDB1L CR for low and high m_{eff} bins are shown. The uncertainty bands plotted include all statistical and systematic uncertainties. The overflow events, where present, are included in the last bin.
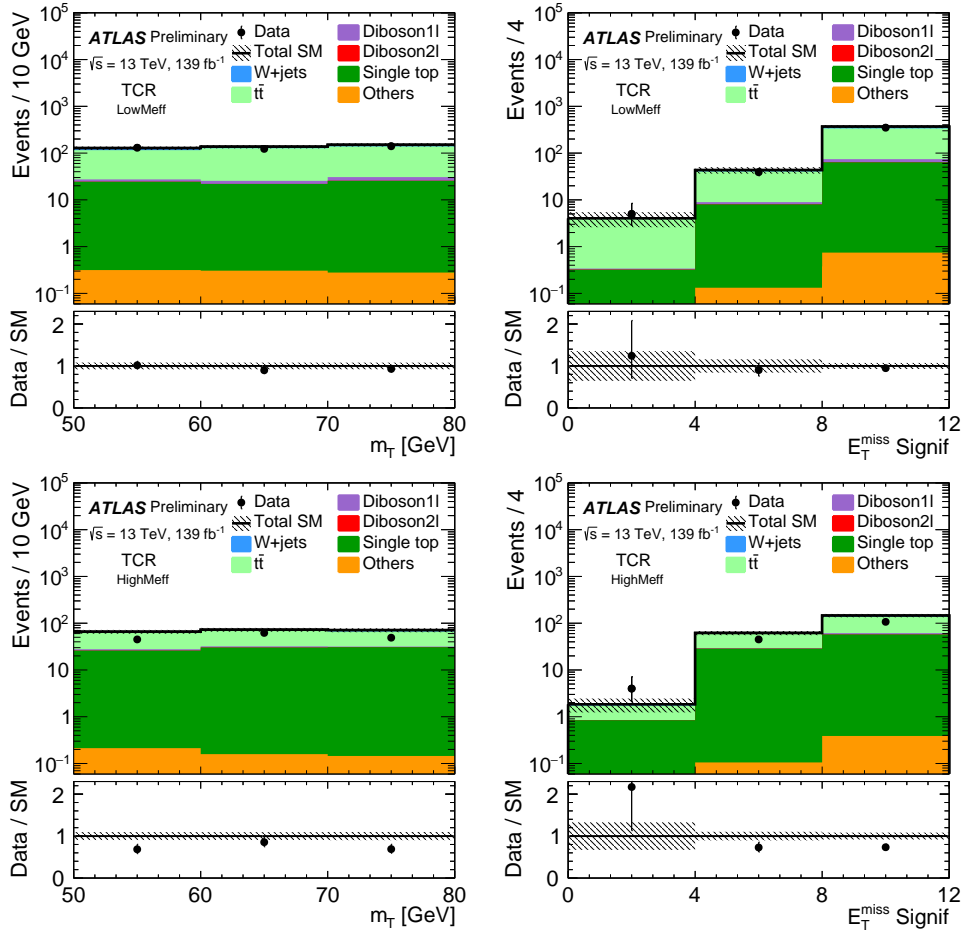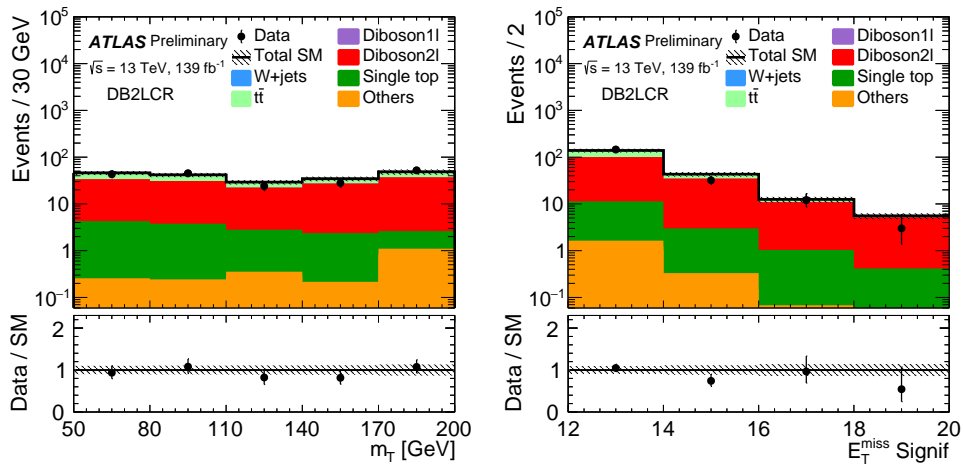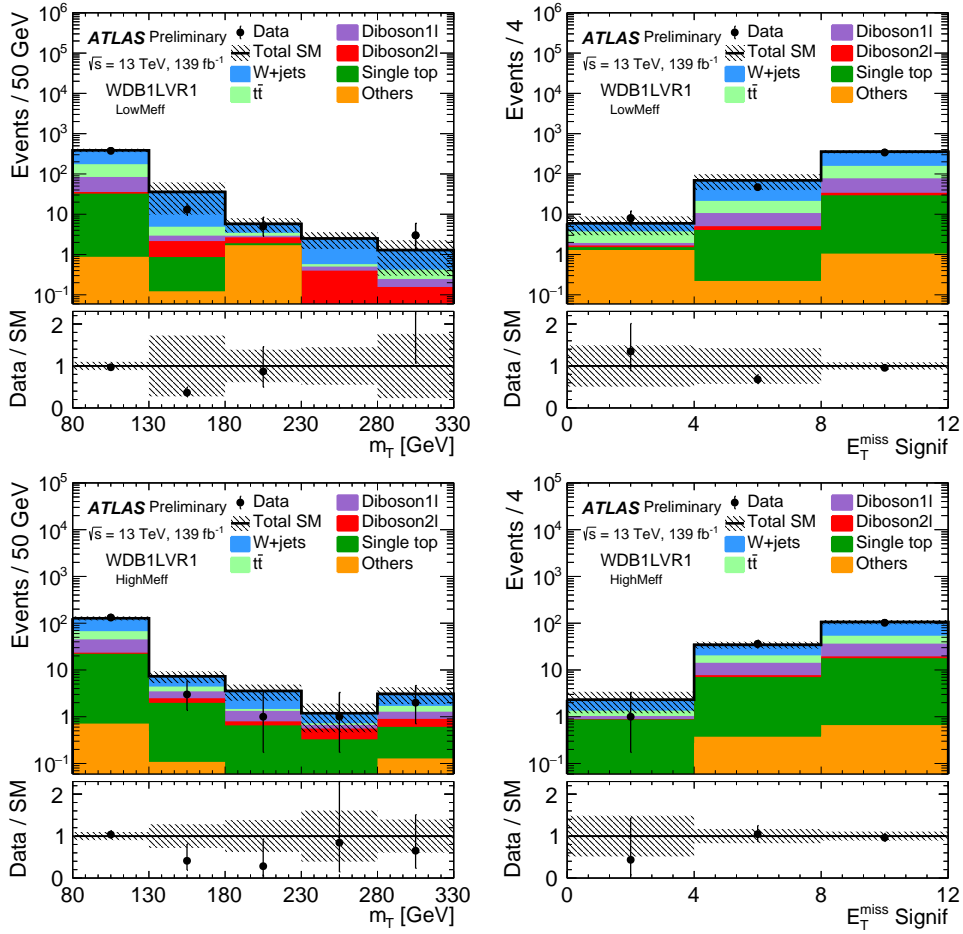
Figure 8: The post-fit m_T and $\sigma_{E_T^{miss}}$ distributions in $t\bar{t}$ CR for low and high m_{eff} bins are shown. The uncertainty bands plotted include all statistical and systematic uncertainties. The overflow events, where present, are included in the last bin.

Figure 9: The post-fit m_T and $\sigma_{E_T^{miss}}$ distributions in DB2L CR for low and high m_{eff} bins are shown. The post-fit distribution for m_{eff} in DB2L CR is also shown. The uncertainty bands plotted include all statistical and systematic uncertainties. The overflow events, where present, are included in the last bin.
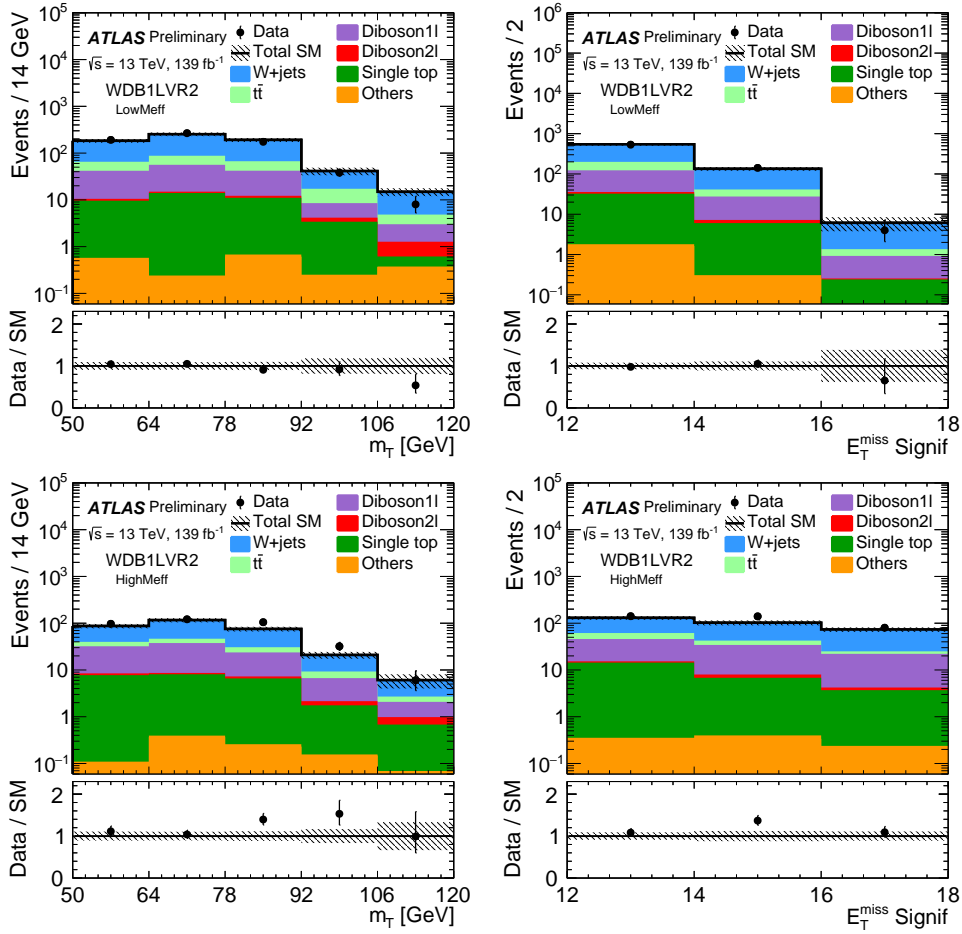
Figure 10: The post-fit m_T and $\sigma_{E_T^{miss}}$ distributions in WDB1L VR1 for low and high m_{eff} bins are shown. The post-fit distribution for m_{eff} is also shown. The uncertainty bands plotted include all statistical and systematic uncertainties. The overflow events, where present, are included in the last bin.
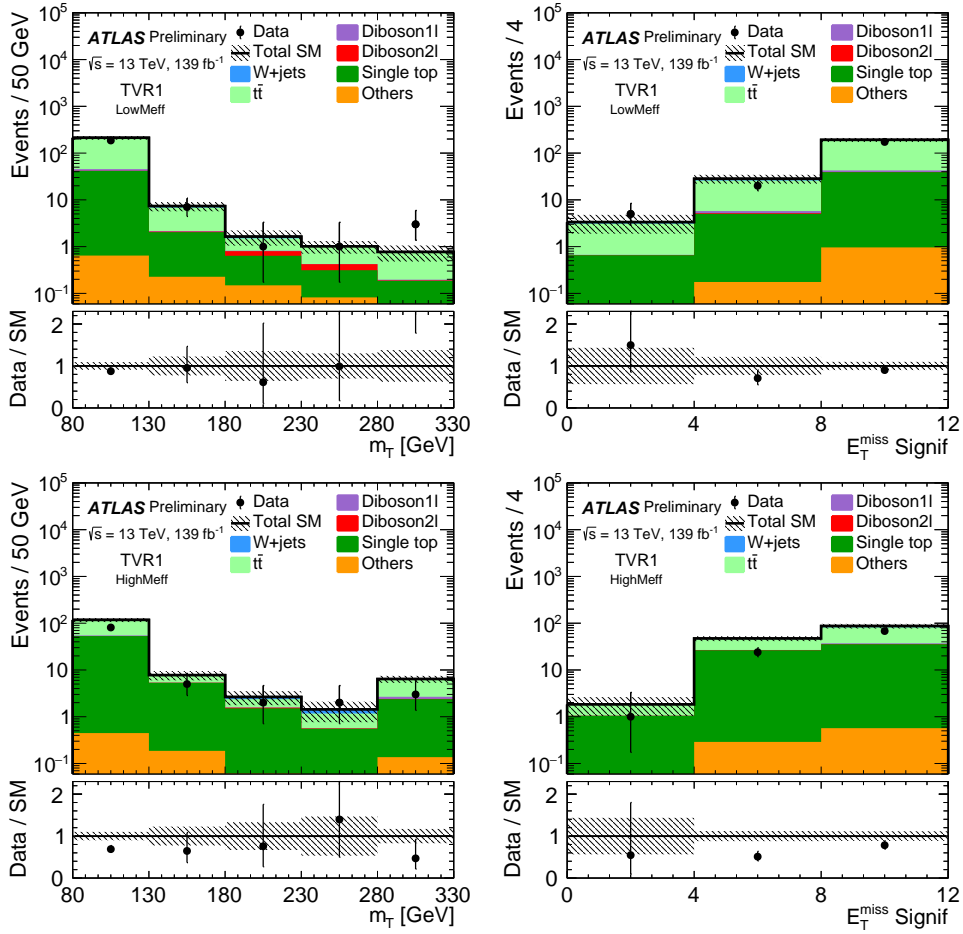
Figure 11: The post-fit m_T and $\sigma_{E_\mathrm{T}^\mathrm{miss}}$ distributions in WDB1L VR2 for low and high m_eff bins are shown. The post-fit distribution for m_eff is also shown. The uncertainty bands plotted include all statistical and systematic uncertainties. The overflow events, where present, are included in the last bin.

Figure 12: The post-fit m_T and $\sigma_{E_T^{miss}}$ distributions in $t\bar{t}$ VR1 for low and high m_{eff} bins are shown. The post-fit distribution for m_{eff} is also shown. The uncertainty bands plotted include all statistical and systematic uncertainties. The overflow events, where present, are included in the last bin.
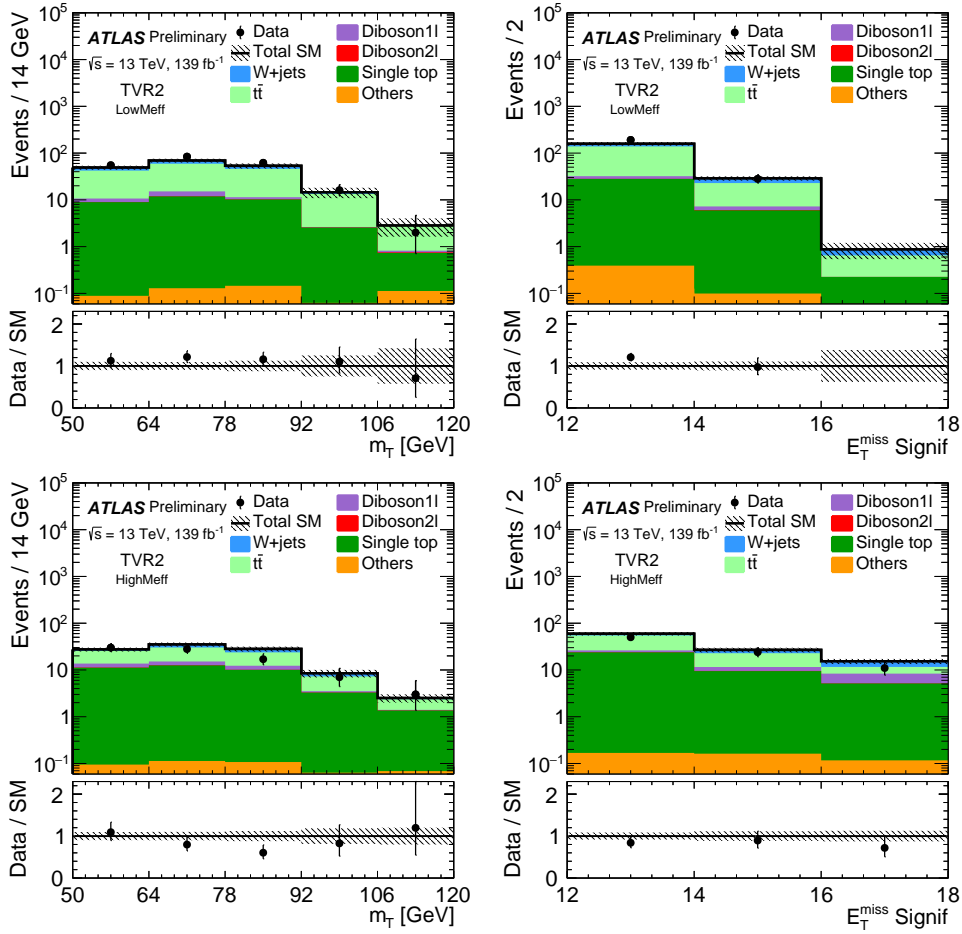
Figure 13: The post-fit m_T and $\sigma_{E_T^{miss}}$ distributions in $t\bar{t}$ VR2 for low and high m_{eff} bins are shown. The post-fit distribution for m_{eff} is also shown. The uncertainty bands plotted include all statistical and systematic uncertainties. The overflow events, where present, are included in the last bin.
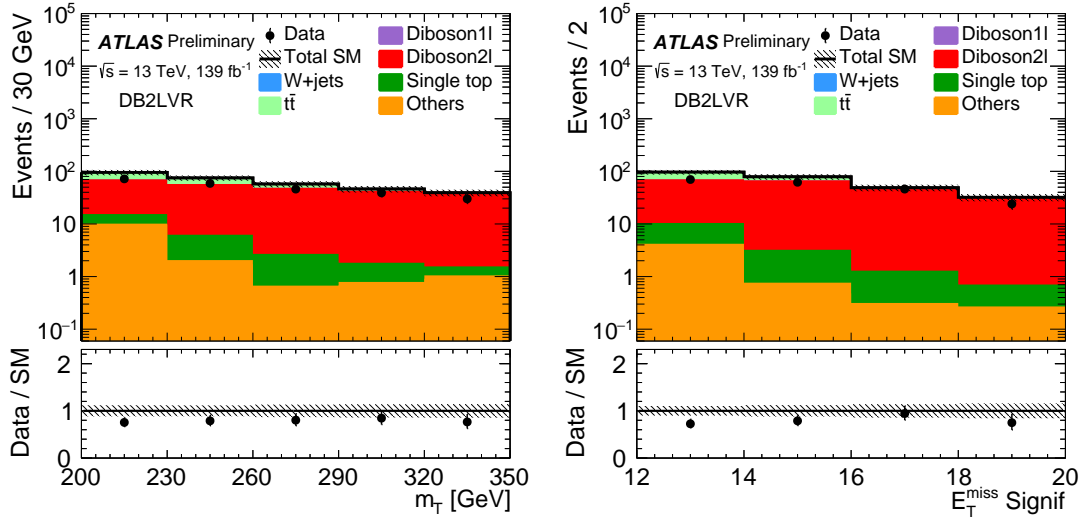
Figure 14: The post-fit m_T and $\sigma_{E_T^{miss}}$ distributions in DB2L validation for low and high m_{eff} bins are shown. The post-fit distribution for m_{eff} is also shown. The uncertainty bands plotted include all statistical and systematic uncertainties. The overflow events, where present, are included in the last bin.
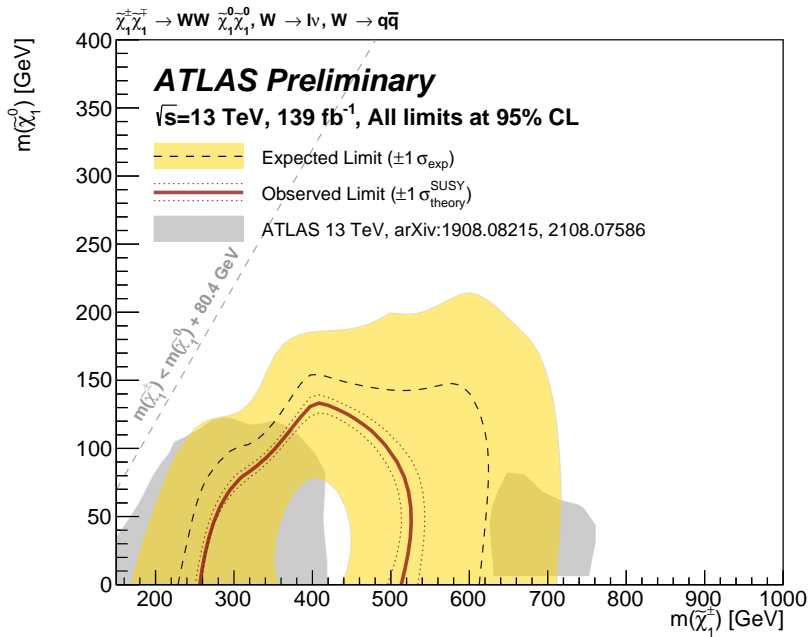

Figure 15: Model-dependent exclusion contour at 95% CL on the chargino pair production. The observed limit is given by the solid line with the signal cross-section uncertainties shown by the dotted lines as indicated in the text. Expected limits are given by the dashed line with uncertainties shown by the shaded band. The Shaded areas represent excluded mass hypotheses from other ATLAS searches.

References

[1] ATLAS Collaboration, *Observation of a new particle in the search for the Standard Model Higgs boson with the ATLAS detector at the LHC*, Phys. Lett. B **716** (2012) 1, arXiv: `1207.7214 [hep-ex]` (cit. on p. 2).

[2] CMS Collaboration, *Observation of a new boson at a mass of 125 GeV with the CMS experiment at the LHC*, Phys. Lett. B **716** (2012) 30, arXiv: `1207.7235 [hep-ex]` (cit. on p. 2).

[3] ATLAS and CMS Collaborations, *Combined Measurement of the Higgs Boson Mass in pp Collisions at $\sqrt{s}$ = 7 and 8 TeV with the ATLAS and CMS Experiments*, Phys. Rev. Lett. **114** (2015) 191803, arXiv: `1503.07589 [hep-ex]` (cit. on p. 2).

[4] ATLAS and CMS Collaborations, *Measurements of the Higgs boson production and decay rates and constraints on its couplings from a combined ATLAS and CMS analysis of the LHC pp collision data at $\sqrt{s}$ = 7 and 8 TeV*, JHEP **08** (2016) 045, arXiv: `1606.02266 [hep-ex]` (cit. on p. 2).

[5] N. Sakai, *Naturalness in supersymmetric GUTS*, Z. Phys. C **11** (1981) 153 (cit. on p. 2).

[6] S. Dimopoulos, S. Raby and F. Wilczek, *Supersymmetry and the scale of unification*, Phys. Rev. D **24** (1981) 1681 (cit. on p. 2).

[7] L. E. Ibanez and G. G. Ross, *Low-energy predictions in supersymmetric grand unified theories*, Phys. Lett. B **105** (1981) 439 (cit. on p. 2).

[8] S. Dimopoulos and H. Georgi, *Softly broken supersymmetry and SU(5)*, Nucl. Phys. B **193** (1981) 150 (cit. on p. 2).

[9] Y. A. Golfand and E. P. Likhtman, *Extension of the Algebra of Poincare Group Generators and Violation of P invariance*, JETP Lett. **13** (1971) 323, [Pisma Zh. Eksp. Teor. Fiz. **13** (1971) 452] (cit. on p. 2).

[10] D. V. Volkov and V. P. Akulov, *Is the neutrino a goldstone particle?*, Phys. Lett. B **46** (1973) 109 (cit. on p. 2).

[11] J. Wess and B. Zumino, *Supergauge transformations in four-dimensions*, Nucl. Phys. B **70** (1974) 39 (cit. on p. 2).

[12] J. Wess and B. Zumino, *Supergauge invariant extension of quantum electrodynamics*, Nucl. Phys. B **78** (1974) 1 (cit. on p. 2).

[13] S. Ferrara and B. Zumino, *Supergauge invariant Yang-Mills theories*, Nucl. Phys. B **79** (1974) 413 (cit. on p. 2).

[14] A. Salam and J. A. Strathdee, *Super-symmetry and non-Abelian gauges*, Phys. Lett. B **51** (1974) 353 (cit. on p. 2).

[15] G. R. Farrar and P. Fayet, *Phenomenology of the production, decay, and detection of new hadronic states associated with supersymmetry*, Phys. Lett. B **76** (1978) 575 (cit. on p. 2).

[16] H. Goldberg, *Constraint on the Photino Mass from Cosmology*, Phys. Rev. Lett. **50** (1983) 1419, [Erratum: Phys. Rev. Lett. **103** (2009) 099905] (cit. on p. 2).

[17] J. R. Ellis, J. S. Hagelin, D. V. Nanopoulos, K. A. Olive and M. Srednicki, *Supersymmetric relics from the big bang*, Nucl. Phys. B **238** (1984) 453 (cit. on p. 2).

[18] R. Barbieri and G. F. Giudice, *Upper bounds on supersymmetric particle masses*,
Nucl. Phys. B **306** (1988) 63 (cit. on p. 2).

[19] B. de Carlos and J. A. Casas, *One loop analysis of the electroweak breaking in supersymmetric models and the fine tuning problem*, Phys. Lett. B **309** (1993) 320,
arXiv: hep-ph/9303291 [hep-ph] (cit. on p. 2).

[20] P. Fayet, *Supersymmetry and Weak, Electromagnetic and Strong Interactions*,
Phys. Lett. B **64** (1976) 159 (cit. on p. 2).

[21] P. Fayet,
Spontaneously broken supersymmetric theories of weak, electromagnetic and strong interactions,
Phys. Lett. B **69** (1977) 489 (cit. on p. 2).

[22] J. Gunion et al., *Calculation and Phenomenology of Two Body Decays of Neutralinos and Charginos to W, Z, and Higgs Bosons*, Int. J. Mod. Phys. A **2** (1987) 1145 (cit. on p. 2).

[23] T. Moroi,
Muon anomalous magnetic dipole moment in the minimal supersymmetric standard model,
Phys. Rev. D **53** (1996) 6565, Erratum: Phys. Rev. D 56 (1997) 4424 (cit. on p. 2).

[24] J. L. Feng and T. Moroi, *Supernatural supersymmetry: Phenomenological implications of anomaly-mediated supersymmetry breaking*, Phys. Rev. D **61** (2000) 095004 (cit. on p. 2).

[25] J. Alwall, P. Schuster and N. Toro,
Simplified models for a first characterization of new physics at the LHC,
Phys. Rev. D **79** (2009) 075020, arXiv: 0810.3921 [hep-ph] (cit. on p. 2).

[26] D. Alves et al., *Simplified models for LHC new physics searches*, J. Phys. G **39** (2012) 105005,
arXiv: 1105.2838 [hep-ph], URL: http://inspirehep.net/record/900212 (cit. on p. 2).

[27] ATLAS Collaboration, *Search for chargino and neutralino production in final states with a Higgs boson and missing transverse momentum at $\sqrt{s} = 13\,TeV$ with the ATLAS detector*,
Phys. Rev. D **100** (2019) 012006, arXiv: 1812.09432 [hep-ex] (cit. on p. 2).

[28] ATLAS Collaboration, *Searches for new phenomena in events with two leptons, jets, and missing transverse momentum in $139\,fb^{-1}$ of $\sqrt{s} = 13\,TeV$ pp collisions with the ATLAS detector*, (2022),
arXiv: 2204.13072 [hep-ex] (cit. on pp. 2, 10).

[29] ATLAS Collaboration,
Search for electroweak production of charginos and sleptons decaying into final states with two leptons and missing transverse momentum in $\sqrt{s} = 13\,TeV$ pp collisions using the ATLAS detector,
Eur. Phys. J. C **80** (2020) 123, arXiv: 1908.08215 [hep-ex] (cit. on pp. 2, 22).

[30] ATLAS Collaboration,
Search for charginos and neutralinos in final states with two boosted hadronically decaying bosons and missing transverse momentum in pp collisions at $\sqrt{s} = 13\,TeV$ with the ATLAS detector,
Phys. Rev. D **104** (2021) 112010, arXiv: 2108.07586 [hep-ex] (cit. on pp. 2, 22).

[31] ATLAS Collaboration,
Search for chargino–neutralino pair production in final states with three leptons and missing transverse momentum in sqrts = 13 TeV pp collisions with the ATLAS detector,
Eur. Phys. J. C **81** (2021) 1118, arXiv: 2106.01676 [hep-ex] (cit. on p. 2).

[32] CMS Collaboration, *Combined search for electroweak production of charginos and neutralinos in proton-proton collisions at $\sqrt{s} = 13\,TeV$*, JHEP **03** (2018) 160, arXiv: 1801.03957 [hep-ex]
(cit. on p. 2).

[33] ATLAS Collaboration, *The ATLAS Experiment at the CERN Large Hadron Collider*,
JINST **3** (2008) S08003 (cit. on p. 3).

[34] ATLAS Collaboration, *ATLAS Insertable B-Layer Technical Design Report*, ATLAS-TDR-19,
2010, URL: https://cds.cern.ch/record/1291633,
ATLAS Insertable B-Layer Technical Design Report Addendum, ATLAS-TDR-19-ADD-1, 2012,
URL: https://cds.cern.ch/record/1451888 (cit. on p. 3).

[35] B. Abbott et al., *Production and integration of the ATLAS Insertable B-Layer*,
JINST **13** (2018) T05008, arXiv: 1803.00844 [physics.ins-det] (cit. on p. 3).

[36] ATLAS Collaboration, *Performance of the ATLAS trigger system in 2015*,
Eur. Phys. J. C **77** (2017) 317, arXiv: 1611.09661 [hep-ex] (cit. on p. 3).

[37] ATLAS Collaboration,
Luminosity determination in pp collisions at $\sqrt{s}$ = 13 TeV using the ATLAS detector at the LHC,
ATLAS-CONF-2019-021, 2019, URL: https://cds.cern.ch/record/2677054 (cit. on p. 4).

[38] G. Avoni et al., *The new LUCID-2 detector for luminosity measurement and monitoring in ATLAS*,
JINST **13** (2018) P07017 (cit. on p. 4).

[39] ATLAS Collaboration, *The ATLAS Simulation Infrastructure*, Eur. Phys. J. C **70** (2010) 823,
arXiv: 1005.4568 [physics.ins-det] (cit. on p. 4).

[40] ATLAS Collaboration, *The ATLAS Collaboration Software and Firmware*,
ATL-SOFT-PUB-2021-001, 2021, URL: https://cds.cern.ch/record/2767187
(cit. on p. 4).

[41] S. Agostinelli et al., *GEANT4 - a simulation toolkit*, Nucl. Instrum. Meth. A **506** (2003) 250
(cit. on p. 4).

[42] ATLAS Collaboration,
The simulation principle and performance of the ATLAS fast calorimeter simulation FastCaloSim,
ATL-PHYS-PUB-2010-013, 2010, URL: https://cds.cern.ch/record/1300517
(cit. on p. 4).

[43] T. Sjöstrand, S. Mrenna and P. Z. Skands, *A brief introduction to PYTHIA 8.1*,
Comput. Phys. Commun. **178** (2008) 852, arXiv: 0710.3820 [hep-ph] (cit. on pp. 4, 5).

[44] R. D. Ball et al., *Parton distributions with LHC data*, Nucl. Phys. B **867** (2013) 244,
arXiv: 1207.1303 [hep-ph] (cit. on pp. 4, 5).

[45] ATLAS Collaboration, *The Pythia 8 A3 tune description of ATLAS minimum bias and inelastic
measurements incorporating the Donnachie–Landshoff diffractive model*,
ATL-PHYS-PUB-2016-017, 2016, URL: https://cds.cern.ch/record/2206965
(cit. on p. 4).

[46] T. Gleisberg and S. Höche, *Comix, a new matrix element generator*, JHEP **12** (2008) 039,
arXiv: 0808.3674 [hep-ph] (cit. on p. 4).

[47] F. Cascioli, P. Maierhöfer and S. Pozzorini, *Scattering Amplitudes with Open Loops*,
Phys. Rev. Lett. **108** (2012) 111601, arXiv: 1111.5206 [hep-ph] (cit. on p. 4).

[48] A. Denner, S. Dittmaier and L. Hofer,
Collier: A fortran-based complex one-loop library in extended regularizations,
Comput. Phys. Commun. **212** (2017) 220, arXiv: 1604.06792 [hep-ph] (cit. on p. 4).

[49] S. Schumann and F. Krauss,
      A parton shower algorithm based on Catani–Seymour dipole factorisation, JHEP **03** (2008) 038,
      arXiv: 0709.1027 [hep-ph] (cit. on p. 4).

[50] S. Höche, F. Krauss, M. Schönherr and F. Siegert,
      A critical appraisal of NLO+PS matching methods, JHEP **09** (2012) 049,
      arXiv: 1111.1220 [hep-ph] (cit. on p. 4).

[51] S. Höche, F. Krauss, M. Schönherr and F. Siegert,
      QCD matrix elements + parton showers. The NLO case, JHEP **04** (2013) 027,
      arXiv: 1207.5030 [hep-ph] (cit. on p. 4).

[52] S. Catani, F. Krauss, B. R. Webber and R. Kuhn, *QCD Matrix Elements + Parton Showers*,
      JHEP **11** (2001) 063, arXiv: hep-ph/0109231 (cit. on p. 4).

[53] S. Höche, F. Krauss, S. Schumann and F. Siegert, *QCD matrix elements and truncated showers*,
      JHEP **05** (2009) 053, arXiv: 0903.1219 [hep-ph] (cit. on p. 4).

[54] D. J. Lange, *The EvtGen particle decay simulation package*,
      Nucl. Instrum. Meth. A **462** (2001) 152 (cit. on p. 4).

[55] L. Lönnblad and S. Prestel, *Merging multi-leg NLO matrix elements with parton showers*,
      JHEP **03** (2013) 166, arXiv: 1211.7278 [hep-ph] (cit. on p. 4).

[56] J. Alwall et al., *The automated computation of tree-level and next-to-leading order differential
      cross sections, and their matching to parton shower simulations*, JHEP **07** (2014) 079,
      arXiv: 1405.0301 [hep-ph] (cit. on p. 4).

[57] ATLAS Collaboration, *ATLAS Pythia 8 tunes to 7 TeV data*, ATL-PHYS-PUB-2014-021, 2014,
      URL: https://cds.cern.ch/record/1966419 (cit. on pp. 4, 5).

[58] J. Debove, B. Fuks and M. Klasen,
      Threshold resummation for gaugino pair production at hadron colliders,
      Nucl. Phys. B **842** (2011) 51, arXiv: 1005.2909 [hep-ph] (cit. on p. 4).

[59] B. Fuks, M. Klasen, D. R. Lamprea and M. Rothering,
      Gaugino production in proton-proton collisions at a center-of-mass energy of 8 TeV,
      JHEP **1210** (2012) 081, arXiv: 1207.2159 [hep-ph] (cit. on p. 4).

[60] B. Fuks, M. Klasen, D. R. Lamprea and M. Rothering, *Precision predictions for electroweak
      superpartner production at hadron colliders with Resummino*, Eur.Phys.J. **C73** (2013) 2480,
      arXiv: 1304.0790 [hep-ph] (cit. on p. 4).

[61] J. Fiaschi and M. Klasen, *Neutralino-chargino pair production at NLO+NLL with
      resummation-improved parton density functions for LHC Run II*, Phys. Rev. D **98** (2018) 055014,
      arXiv: 1805.11322 [hep-ph] (cit. on p. 4).

[62] C. Borschensky et al.,
      Squark and gluino production cross sections in pp collisions at $\sqrt{s}$ = 13, 14, 33 and 100 TeV,
      Eur. Phys. J. C **74** (2014) 3174, arXiv: 1407.5066 [hep-ph] (cit. on p. 4).

[63] S. Alioli, P. Nason, C. Oleari and E. Re, *A general framework for implementing NLO calculations
      in shower Monte Carlo programs: the POWHEG BOX*, JHEP **06** (2010) 043,
      arXiv: 1002.2581 [hep-ph] (cit. on p. 5).

[64] S. Frixione, P. Nason and C. Oleari,
      Matching NLO QCD computations with parton shower simulations: the POWHEG method,
      JHEP **11** (2007) 070, arXiv: 0709.2092 [hep-ph] (cit. on p. 5).

[65] S. Frixione, P. Nason and G. Ridolfi,
A positive-weight next-to-leading-order Monte Carlo for heavy flavour hadroproduction,
JHEP **09** (2007) 126, arXiv: `0707.3088 [hep-ph]` (cit. on p. 5).

[66] P. Nason, *A new method for combining NLO QCD with shower Monte Carlo algorithms*,
JHEP **11** (2004) 040, arXiv: `hep-ph/0409146` (cit. on p. 5).

[67] M. Czakon and A. Mitov,
Top++: A program for the calculation of the top-pair cross-section at hadron colliders,
Comput. Phys. Commun. **185** (2014) 2930, arXiv: `1112.5675 [hep-ph]` (cit. on p. 5).

[68] E. Re,
Single-top Wt-channel production matched with parton showers using the POWHEG method,
Eur. Phys. J. C **71** (2011) 1547, arXiv: `1009.2450 [hep-ph]` (cit. on p. 5).

[69] R. Frederix, E. Re and P. Torrielli,
Single-top t-channel hadroproduction in the four-flavour scheme with POWHEG and aMC@NLO,
JHEP **09** (2012) 130, arXiv: `1207.5391 [hep-ph]` (cit. on p. 5).

[70] S. Alioli, P. Nason, C. Oleari and E. Re,
NLO single-top production matched with shower in POWHEG: s- and t-channel contributions,
JHEP **09** (2009) 111, [Erratum: JHEP02,011(2010)], arXiv: `0907.4076 [hep-ph]` (cit. on p. 5).

[71] M. Aliev et al., *HATHOR – HAdronic Top and Heavy quarks crOss section calculatoR*,
Comput. Phys. Commun. **182** (2011) 1034, arXiv: `1007.1327 [hep-ph]` (cit. on p. 5).

[72] T. Gleisberg et al., *Event generation with SHERPA 1.1*, JHEP **02** (2009) 007,
arXiv: `0811.4622 [hep-ph]` (cit. on p. 5).

[73] C. Anastasiou, L. J. Dixon, K. Melnikov and F. Petriello,
High precision QCD at hadron colliders: Electroweak gauge boson rapidity distributions at NNLO,
Phys. Rev. D **69** (2004) 094008, arXiv: `hep-ph/0312266` (cit. on p. 5).

[74] P. Bärnreuther, M. Czakon and A. Mitov, *Percent Level Precision Physics at the Tevatron: First
Genuine NNLO QCD Corrections to $q\bar{q} \rightarrow t\bar{t} + X$*, Phys. Rev. Lett. **109** (2012) 132001,
arXiv: `1204.5201 [hep-ph]` (cit. on p. 5).

[75] ATLAS Collaboration, *Measurement of the Z/γ^* boson transverse momentum distribution in pp
collisions at $\sqrt{s}$ = 7 TeV with the ATLAS detector*, JHEP **09** (2014) 145,
arXiv: `1406.3660 [hep-ex]` (cit. on p. 5).

[76] P. M. Nadolsky et al., *Implications of CTEQ global analysis for collider observables*,
Phys. Rev. D **78** (2008) 013004, arXiv: `0802.0007 [hep-ph]` (cit. on p. 5).

[77] D. de Florian et al.,
Handbook of LHC Higgs cross sections: 4. Deciphering the nature of the Higgs sector,
CERN-2017-002-M (2016), arXiv: `1610.07922 [hep-ph]` (cit. on p. 5).

[78] ATLAS Collaboration, *Vertex Reconstruction Performance of the ATLAS Detector at $\sqrt{s}$ = 13 TeV*,
ATL-PHYS-PUB-2015-026, 2015, URL: `https://cds.cern.ch/record/2037717`
(cit. on p. 5).

[79] ATLAS Collaboration,
Selection of jets produced in 13 TeV proton–proton collisions with the ATLAS detector,
ATLAS-CONF-2015-029, 2015, URL: `https://cds.cern.ch/record/2037702` (cit. on p. 5).

[80] ATLAS Collaboration, *Electron and photon performance measurements with the ATLAS detector using the 2015-2017 LHC proton-proton collision data*, (2019), arXiv: 1908.00005 [hep-ex] (cit. on p. 5).

[81] A. Collaboration, *Evidence for the associated production of the Higgs boson and a top quark pair with the ATLAS detector*, Phys. Rev. D **97** (7 2018) 072003, URL: https://link.aps.org/doi/10.1103/PhysRevD.97.072003 (cit. on pp. 5, 6).

[82] ATLAS Collaboration, *Muon reconstruction performance of the ATLAS detector in proton–proton collision data at $\sqrt{s}$ = 13 TeV*, Eur. Phys. J. C **76** (2016) 292, arXiv: 1603.05598 [hep-ex] (cit. on pp. 5, 12).

[83] ATLAS Collaboration, *Topological cell clustering in the ATLAS calorimeters and its performance in LHC Run 1*, Eur. Phys. J. C **77** (2017) 490, arXiv: 1603.02934 [hep-ex] (cit. on p. 6).

[84] M. Cacciari, G. P. Salam and G. Soyez, *The anti-k_t jet clustering algorithm*, JHEP **04** (2008) 063, arXiv: 0802.1189 [hep-ph] (cit. on p. 6).

[85] ATLAS Collaboration, *Performance of pile-up mitigation techniques for jets in pp collisions at $\sqrt{s}$ = 8 TeV using the ATLAS detector*, Eur. Phys. J. C **76** (2016) 581, arXiv: 1510.03823 [hep-ex] (cit. on p. 6).

[86] M. Cacciari, G. P. Salam and G. Soyez, *FastJet user manual*, Eur. Phys. J. C **72** (2012) 1896, arXiv: 1111.6097 [hep-ph] (cit. on p. 6).

[87] ATLAS Collaboration, *Jet Calibration and Systematic Uncertainties for Jets Reconstructed in the ATLAS Detector at $\sqrt{s}$ = 13 TeV*, ATL-PHYS-PUB-2015-015, 2015, URL: https://cds.cern.ch/record/2037613 (cit. on p. 6).

[88] D. Krohn, J. Thaler and L.-T. Wang, *Jet trimming*, JHEP **02** (2010) 084, arXiv: 0912.1342 [hep-ph] (cit. on p. 6).

[89] ATLAS Collaboration, *Jet mass reconstruction with the ATLAS Detector in early Run 2 data*, ATLAS-CONF-2016-035, 2016, URL: https://cds.cern.ch/record/2200211 (cit. on p. 6).

[90] ATLAS Collaboration, *Performance of top-quark and W-boson tagging with ATLAS in Run 2 of the LHC*, Eur. Phys. J. C **79** (2019) 375, arXiv: 1808.07858 [hep-ex] (cit. on p. 6).

[91] ATLAS Collaboration, *Boosted hadronic vector boson and top quark tagging with ATLAS using Run 2 data*, ATL-PHYS-PUB-2020-017, 2020, URL: https://cds.cern.ch/record/2724149 (cit. on p. 6).

[92] ATLAS Collaboration, *Identification of Jets Containing b-Hadrons with Recurrent Neural Networks at the ATLAS Experiment*, ATL-PHYS-PUB-2017-003, 2017, URL: https://cds.cern.ch/record/2255226 (cit. on p. 6).

[93] M. Cacciari, G. P. Salam and G. Soyez, *The catchment area of jets*, JHEP **04** (2008) 005, arXiv: 0802.1188 [hep-ph] (cit. on p. 6).

[94] ATLAS Collaboration, *Measurement of the photon identification efficiencies with the ATLAS detector using LHC Run 2 data collected in 2015 and 2016*, Eur. Phys. J. C **79** (2019) 205, arXiv: 1810.05087 [hep-ex] (cit. on p. 6).

[95] ATLAS Collaboration, *Performance of missing transverse momentum reconstruction with the ATLAS detector using proton–proton collisions at* $\sqrt{s}$ = 13 *TeV*, Eur. Phys. J. C **78** (2018) 903, arXiv: 1802.08168 [hep-ex] (cit. on p. 6).

[96] ATLAS Collaboration, E_T^{miss} *performance in the ATLAS detector using 2015–2016 LHC pp collisions*, ATLAS-CONF-2018-023, 2018, URL: https://cds.cern.ch/record/2625233 (cit. on pp. 6, 12).

[97] ATLAS Collaboration, *Performance of the ATLAS muon triggers in Run 2*, JINST **15** (2020) P09015, arXiv: 2004.13447 [hep-ex] (cit. on p. 6).

[98] ATLAS Collaboration, *Performance of electron and photon triggers in ATLAS during LHC Run 2*, Eur. Phys. J. C **80** (2020) 47, arXiv: 1909.00761 [hep-ex] (cit. on p. 6).

[99] ATLAS Collaboration, *Object-based missing transverse momentum significance in the ATLAS Detector*, ATLAS-CONF-2018-038, 2018, URL: https://cds.cern.ch/record/2630948 (cit. on p. 7).

[100] T. Gillam and C. Lester, *Improving estimates of the number of 'fake' leptons and other mis-reconstructed objects in hadron collider events: BoB's your UNCLE*, JHEP **11** (2014) 031, arXiv: 1407.5624 [hep-ph] (cit. on p. 11).

[101] J. Bellm et al., *Herwig 7.0/Herwig++ 3.0 release note*, Eur. Phys. J. **C76** (2016) 196, arXiv: 1512.01178 [hep-ph] (cit. on p. 12).

[102] ATLAS Collaboration, *Simulation of top-quark production for the ATLAS experiment at* $\sqrt{s}$ = 13 *TeV*, ATL-PHYS-PUB-2016-004, 2016, URL: https://cds.cern.ch/record/2120417 (cit. on p. 12).

[103] J. Butterworth et al., *PDF4LHC recommendations for LHC Run II*, J. Phys. G **43** (2016) 023001, arXiv: 1510.03865 [hep-ph] (cit. on p. 12).

[104] ATLAS Collaboration, *Multi-boson simulation for* 13 *TeV ATLAS analyses*, ATL-PHYS-PUB-2016-002, 2016, URL: https://cds.cern.ch/record/2119986 (cit. on p. 12).

[105] ATLAS Collaboration, *Jet energy scale measurements and their systematic uncertainties in proton–proton collisions at* $\sqrt{s}$ = 13 *TeV with the ATLAS detector*, Phys. Rev. D **96** (2017) 072002, arXiv: 1703.09665 [hep-ex] (cit. on p. 12).

[106] ATLAS Collaboration, *Electron and photon performance measurements with the ATLAS detector using the 2015–2017 LHC proton–proton collision data*, JINST **14** (2019) P12006, arXiv: 1908.00005 [hep-ex] (cit. on p. 12).

[107] R. D. Cousins, J. T. Linnemann and J. Tucker, *Evaluation of three methods for calculating statistical significance when incorporating a systematic uncertainty into a test of the background-only hypothesis for a Poisson process*, Nucl. Instrum. Meth. A **595** (2008) 480, arXiv: physics/0702156 [physics.data-an] (cit. on p. 21).

[108] A. L. Read, *Presentation of search results: The* CL_S *technique*, J. Phys. G **28** (2002) 2693 (cit. on p. 22).